

## Accepted Manuscript

Elastic instabilities in pressure-driven channel flow of thixotropic-viscoelasto-plastic fluids

Hugo A. Castillo, Helen J. Wilson

PII: S0377-0257(18)30188-5  
DOI: <https://doi.org/10.1016/j.jnnfm.2018.07.009>  
Reference: JNNFM 4034



To appear in: *Journal of Non-Newtonian Fluid Mechanics*

Received date: 25 May 2018  
Revised date: 26 July 2018  
Accepted date: 31 July 2018

Please cite this article as: Hugo A. Castillo, Helen J. Wilson, Elastic instabilities in pressure-driven channel flow of thixotropic-viscoelasto-plastic fluids, *Journal of Non-Newtonian Fluid Mechanics* (2018), doi: <https://doi.org/10.1016/j.jnnfm.2018.07.009>

This is a PDF file of an unedited manuscript that has been accepted for publication. As a service to our customers we are providing this early version of the manuscript. The manuscript will undergo copyediting, typesetting, and review of the resulting proof before it is published in its final form. Please note that during the production process errors may be discovered which could affect the content, and all legal disclaimers that apply to the journal pertain.

## Highlights

- We use the Bautista-Manero-Puig model to investigate channel ow instabilities.
- Instability is seen when viscoelastic effects dominate; thixotropy is stabilising.
- Very unstable ows have the low to high shear transition point near the wall.
- The thixotropic structure recovery rate determines the growth rate of instability.
- We predict a critical wall shear stress that is in agreement with experiments.

# Elastic instabilities in pressure-driven channel flow of thixotropic-viscoelasto-plastic fluids

Hugo A. Castillo and Helen J. Wilson  
*Mathematics Department, University College London  
Gower Street, London WC1E 6BT, UK*

August 6, 2018

---

## Abstract

We study the stability of pressure-driven channel flow of a thixotropic-viscoelasto-plastic fluid. Several recent experiments have shown that channel flows of shear-thinning polymer solutions can be linearly unstable even at very low Reynolds numbers. We use the Bautista–Manero–Puig model (BMP) to attempt to capture the physics of these instabilities. We obtain an analytic solution for the steady-state velocity profile, dependent on our fluid parameters, that is able to predict a large variety of base states. We derive dimensionless groups to compare the effects of viscoelasticity, thixotropy and plasticity on the flow stability. We find that sinuous perturbations are slightly more unstable than varicose modes, and we identify the values of our model parameters for which the instability has its strongest effects. We conclude that dominant thixotropy can stabilise the flow, but instability occurs when the characteristic timescale of viscoelasticity is much longer than both those of plasticity and thixotropy. The most dangerous situation is a plug flow with an apparent yield surface just within the channel, and we find that the growth rate of the instability scales with the rate of thixotropic structure recovery.

---

## 1 Introduction

In recent years, it has been shown that viscoelastic fluids exhibit instabilities in inertialess flows that are not seen in Newtonian fluids: these are commonly described as *elastic instabilities*. Petrie and Denn [25] were the first to identify such instabilities arising in extensional and shearing flows in polymer processing operations. Since then, extensive theoretical and experimental research has

been made by rheologists in order to understand the mechanisms behind these instabilities.

Several categories of elastic instabilities are more or less understood: curved streamline [11, 12], interfacial [13, 14] and shear-banding [15] instabilities. Early work by Wilson and Rallison [3] predicted theoretically an instability that had not previously been seen, for pressure-driven channel flows of highly shear-thinning viscoelastic fluids having a constant elastic modulus and a single polymer relaxation time that depends instantaneously on the shear rate. No experimental evidence of this instability was found until 2015, when Bodiguel and his team [2] demonstrated an elastic instability, occurring at a reproducible critical flow rate, in a channel flow of a high molecular weight polymer solution ( $18 \times 10^6$  g/mol partially hydrolysed polyacrylamide in water) having neither curved streamlines, nor an interface, nor any evidence of shear-banding. Similar results were seen in experiments by Poole [16] in 2016, who also identified an instability for a shear-thinning viscoelastic polymer (1% polyacrylamide). However, theoretical work at that stage was restricted to a very simple model which could not capture the non-constant shear modulus of Bodiguel's polymer.

The theoretical work was subsequently extended by [4] and [5] to couple shear and normal stresses and incorporate a solvent viscosity. However, all these studies were restricted to instability modes with no cross-channel motion at the centreline because of their use of power-law rheometric functions. An additional issue is that the models they used have fluid properties (such as the relaxation time) that depend instantaneously on the flow environment. Therefore in this paper we consider a *structural* parameter (such as molecular entanglements, network junctions, or micelle length) that is changing with deformation history and on which the material properties depend. A finite value of the zero shear viscosity will permit cross-channel motion at the centreline, and the model also captures more complex rheological behaviours: thixotropic-viscoelasto-plasticity. Our chosen model, which satisfies all these requirements, is the BMP model [1], a structural model which has been proven to accurately reproduce the complex rheological behaviour of viscoelastic systems that also exhibit plasticity and thixotropy. In addition, the model is capable of matching the flow curve of shear-thickening and shear-thinning fluids, non-vanishing normal stress differences, shear-banding [18] and even yield stress behaviour [19].

A paper similar to our research presented here was recently published by Renardy [22], who studied the linear stability of a shear-banded flow with viscoelasticity and thixotropic yield stress behaviour in a two-dimensional plane Couette flow; they identified bulk instabilities in the yielded phase (high shear rate zone) along with long wave interfacial instabilities.

In this work, we will stay away from shear-banded flows and focus on identifying only bulk instabilities present in thixotropic-viscoelasto-plastic materials in pressure-driven channel flows. In section 2 we introduce the simplest version of the BMP model and the behaviour of our fluid in steady simple shear. We derive dimensionless equations and construct a group of dimensionless num-

bers recently proposed by Ewoldt [6] that allow us to compare the effects of thixotropy, viscoelasticity and plasticity in our fluid. In section 3 we obtain an analytic solution for the velocity profile, and derive the perturbed governing equations for linear stability analysis. In section 4 we present our results and discuss them in terms of the dimensionless groups introduced in section 2. Finally, in sections 5 and 6, we make general observations and draw our conclusions.

## 2 Model fluid: The BMP model

Many of the materials we use in our daily life — such as foods, personal care products, paints, ink, adhesives, waxy oils, gels, biological fluids such as blood, and pharmaceuticals — fall into the category of *thixotropic-viscoelastoplastic* materials (TVEP). These are structured fluids that display a combination of three time-dependent complex rheological behaviours: viscoelasticity, thixotropy and plasticity. Unlike Newtonian fluids (that simply consist of an homogeneous phase), these kinds of materials are usually composed of multiple phases, such as solid particles or a microstructure dispersed in a viscous (or viscoelastic) continuous phase. The rheological response of these structured fluids usually depend on multiple *characteristic time scales* of the material and on the level of deformation imposed.

TVEP materials show a complex combination of rheological behaviours. Under steady shear, the microstructure will reach a steady configuration that is determined by an equilibrium between the microstructure breakdown and build up processes. After a step change of either shear rate or shear stress, they may exhibit time dependence if a new equilibrium is not reached instantaneously. Above some threshold shear rate or shear stress, they can show microstructure collapse, with a dramatic drop in both elasticity and viscosity; and of course the viscoelastic nature of the fluid can both store energy elastically and dissipate it through viscosity. The mathematical modelling of this kind of fluid is challenging, but there has been progress in recent years. Most models rely on introducing a *structural* parameter, used as a measure of the microstructure, which evolves according to a kinetic equation including both breakdown and buildup processes.

Care needs to be taken when modelling these fluids, to distinguish the effects of thixotropy from nonlinear viscoelasticity. Thixotropy is often defined as a reversible decrease in viscosity over time during flow, but Larson [7] argues that we should instead define thixotropy as a memory that viscosity has of past *strain rate*, and viscoelasticity as a memory that stress has of past *strain*.

Existing TVEP models have been grouped by de Sousa Mendes [10] into two types. Type I models are based on the Bingham model, with thixotropy and viscoelasticity are introduced (as in [24]). On the other hand, Type II models incorporate thixotropy into a viscoelastic stress equation based on the Maxwell

model. For these models, no additional equations are required to describe plasticity, as it is implicitly introduced by expressing the bulk model parameters as a function of the level of structure (when the fluid is completely structured, the viscosity is unbounded). Type II models are more robust than Type I, and are able to describe a wider range of cases, including viscoelasto-plastic fluids with no thixotropy, inelastic thixotropic viscoplastic materials, and of course, thixotropic viscoelasto-plastic or viscoelasto thixo-plastic fluids.

There are several Type II models available in the literature that can successfully describe TVEP behaviour, including de Sousa Mendes' [23] thirteen-parameter model, which is commonly used in the oil and polymer industry due to its ability to model multiple rheological flows. Seeking a simpler model that can still distinguish between thixotropy and nonlinear viscoelasticity, we select the Bautista–Manero–Puig (BMP) model [1]. The BMP model can accurately describe rheological flows of associative polymers, worm-like micellar solutions, dispersions of lamellar liquid crystals, and blood. It has five rheological parameters, which can be estimated from simple rheological experiments in steady and unsteady flows. For various choices of the parameters, it can reproduce shear thinning or shear thickening behaviour, apparent yield stress and actual yield stress.

The simplest version of the model consists of a coupled system of equations: the Upper Convected Maxwell constitutive equation, which calculates the polymer contribution to the stress tensor, along with a kinetic equation proposed by Fredrickson [8], which introduces a *structural parameter*. In thixotropic systems it is observed that the instantaneous rheological properties (such as viscosity) depend on the level of internal structure of the system, and this level changes with deformation history. The evolution of the internal microstructure of the fluid (and therefore, the viscosity) depends on the balance between two processes. The first, *structural reformation* (or *spontaneous build up of viscosity*), occurs whenever the fluid is not perfectly structured, at a rate that is assumed to be independent of the rate at which shear work is done on the material, but instead depends on a characteristic recovery timescale of the material. The second process, *structural destruction* (or *breakdown of viscosity*), occurs only under flow, at a rate that depends on the shear work applied to the material. Fredrickson [8] initially coupled his kinetic equation with a Newtonian stress equation to predict inelastic thixotropic behaviour of suspensions under shear flow. Bautista and colleagues [1] simply introduced the Upper-Convected Maxwell model instead of the Newtonian constitutive equation to incorporate nonlinear viscoelasticity.

A family of models originating from the BMP model have been developed in recent years, introducing extra parameters to predict even more complex rheological phenomena. Examples include shear-banding flows in wormlike micellar solutions [18], and diffusion of species [26]. For the current work we have selected the original BMP for simplicity, and in order to focus on bulk, rather than interfacial, instabilities. Another complication we can avoid is the addition of a

solvent viscosity, as it has been shown in our previous work [5] that the addition of an inelastic solvent stabilises the flow. Although we will not consider shear banding effects, the model we use is still valid for, for instance, micellar systems above the critical temperature, for which shear-banding is not observed [17].

## 2.1 Governing equations

The stress tensor  $\underline{\underline{\sigma}}$  for a BMP fluid flowing with velocity  $\underline{u}$  evolves according to the UCM model:

$$\underline{\underline{\sigma}} + \frac{1}{G_0\varphi} \overset{\nabla}{\underline{\underline{\sigma}}} = \frac{2}{\varphi} \underline{\underline{D}}, \quad (1)$$

in which the upper-convected derivative is defined as

$$\overset{\nabla}{\underline{\underline{\sigma}}} = \frac{D\underline{\underline{\sigma}}}{Dt} - \underline{\underline{\sigma}} \cdot (\nabla \underline{u}) - (\nabla \underline{u})^\top \cdot \underline{\underline{\sigma}}, \quad (2)$$

and  $D/Dt$  denotes the material derivative (for any scalar, vector or tensor quantity  $A$ ):

$$\frac{DA}{Dt} = \frac{\partial A}{\partial t} + \underline{u} \cdot \nabla A, \quad (3)$$

and  $\underline{\underline{D}}$  is the symmetric part of the flow gradient tensor:

$$\underline{\underline{D}} = \frac{1}{2} [\nabla \underline{u} + \nabla \underline{u}^\top] \quad D_{ij} = \frac{1}{2} \left[ \frac{\partial u_i}{\partial x_j} + \frac{\partial u_j}{\partial x_i} \right]. \quad (4)$$

The parameters here are  $G_0$ , the stress modulus, and the variable  $\varphi$ , which is our structural parameter called *fluidity*, simply defined as the inverse of the viscosity ( $\equiv \eta$ ). It evolves according to Fredrickson's equation:

$$\frac{D\varphi}{Dt} = \frac{1}{\lambda} (\varphi_0 - \varphi) + K_0 (\varphi_\infty - \varphi) \underline{\underline{\sigma}} : \underline{\underline{D}}, \quad (5)$$

The right hand side of (5) consists of two terms: the reformation process (build up of viscosity or breakdown of fluidity), parametrised by  $\lambda$ , the *structural relaxation time* and  $\varphi_0$ , the plateau fluidity observed at low shear rates; and the destruction process (breakdown of viscosity or build up of fluidity), described by  $K_0$ , a rate parameter for structure destruction,  $\varphi_\infty$ , the fluidity at high shear rates, and  $\sigma_{ij} D_{ij}$ , the rate of energy dissipation in the fluid.

Equations (1) and (5) are then coupled with the continuity and momentum equations, which are (in the absence of external forces such as gravity):

$$\nabla \cdot \underline{u} = 0 \quad (6)$$

$$\rho \left( \frac{\partial \underline{u}}{\partial t} + \underline{u} \cdot \nabla \underline{u} \right) = -\nabla P + \nabla \cdot \underline{\underline{\sigma}}, \quad (7)$$

where  $\rho$  is the fluid density and  $P$  is the pressure.

## 2.2 Behaviour in steady simple shear

For simple steady shear flow, given in cartesian coordinates by  $\underline{u} = \dot{\gamma}y\mathbf{e}_x$  with  $\dot{\gamma} > 0$ , equations (1) and (5) give:

$$\underline{\underline{\sigma}} = \begin{pmatrix} 2\dot{\gamma}^2 G_0^{-1} \varphi^{-2} & \varphi^{-1} \dot{\gamma} \\ \varphi^{-1} \dot{\gamma} & 0 \end{pmatrix}, \quad (8)$$

$$0 = \frac{1}{\lambda}(\varphi_0 - \varphi) + K_0(\varphi_\infty - \varphi) \frac{\dot{\gamma}^2}{\varphi}. \quad (9)$$

Equation (9) is a quadratic equation for the fluidity, whose solution is:

$$\varphi = \frac{-(K_0 \lambda \dot{\gamma}^2 - \varphi_0) \pm \sqrt{(K_0 \lambda \dot{\gamma}^2 - \varphi_0)^2 + 4(K_0 \lambda \dot{\gamma}^2 \varphi_\infty)}}{2}, \quad (10)$$

For a given set of parameters  $K_0$ ,  $\lambda$ ,  $\varphi_0$  and  $\varphi_\infty$ , equation (10) has exactly one real positive root. If the product  $K_0 \lambda$  is zero (this is *no destruction of structure*), we have a simple Maxwell fluid with constant viscosity  $\eta_0$  ( $\equiv \varphi_0^{-1}$ ). On the other hand, if the product  $K_0 \lambda \rightarrow \infty$  (this is *dominant reformation of structure*), we reach the other extreme  $\varphi = \varphi_\infty$  for any nonzero shear rate.

The viscometric functions (viscosity  $\eta$ , shear stress  $\sigma_{12}$  and the first normal stress difference coefficient  $\Psi_1$ ) are given as:

$$\eta = \varphi^{-1} \quad \sigma_{12} = \eta \dot{\gamma} \quad \Psi_1 = \frac{\sigma_{11} - \sigma_{22}}{\dot{\gamma}^2} = 2G_0^{-1} \eta^2. \quad (11)$$

Figure 1 illustrates the behaviour of these viscometric functions with shear rate, using parameter values  $\varphi_\infty = 15 \text{ Pa}^{-1} \text{ s}^{-1}$ ,  $\varphi_0 = 1.3 \text{ Pa}^{-1} \text{ s}^{-1}$ ,  $G_0 = 68 \text{ Pa}$  and  $K_0 \lambda = 7 \times 10^{-6} \text{ Pa}^{-1} \text{ s}$  chosen to fit a shear-thinning low-concentration micellar solution of CTAT above the shear-banding temperature [17].

### 2.2.1 Shear viscosity and critical shear stress

Figure 1(a) shows the nonlinear global behaviour of the shear stress as a function of shear rate. There are two distinct Newtonian-like regions, which correspond (figure 1(b)) to regions of near-constant fluidity. The low-shear rate phase of complex entangled networks (fully structured state) has  $\varphi \approx \varphi_0$ , and the unstructured state (or highly oriented flow region) has  $\varphi \approx \varphi_\infty$ . The shear stress is a monotonic function of shear rate, and for moderate shear rates there is a small *transition zone* between the phases.

Fredrickson [8] observed that under the sudden startup of shear (with imposed shear stress) there are two different types of behaviour: *primary creep*, at low shear stress, in which the strain rate decreases over time; and *accelerating flow*, in which the strain rate increases monotonically towards its steady

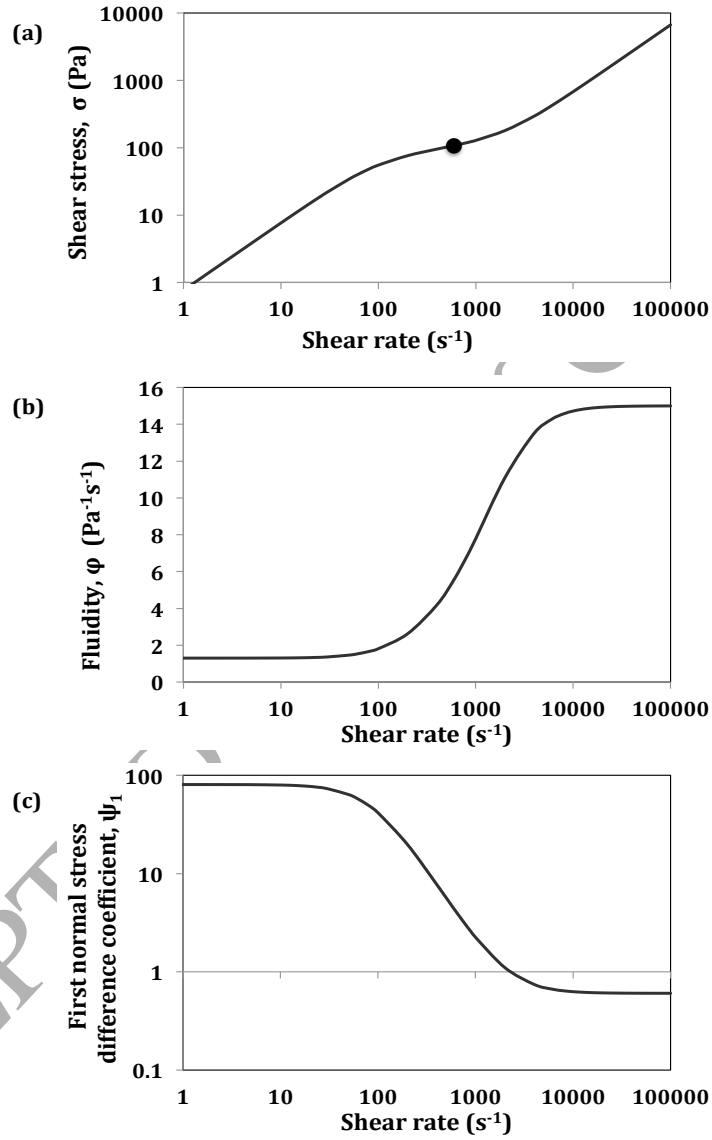


Figure 1: Plots of viscometric functions against shear rate for the BMP model: (a) shear stress, (b) fluidity and (c) first normal stress difference coefficient. In all cases,  $\varphi_{\infty} = 15 Pa^{-1}s^{-1}$ ,  $\varphi_0 = 1.3 Pa^{-1}s^{-1}$ ,  $G_0 = 68 Pa$ , and  $K_0\lambda = 7 \times 10^{-6} Pa^{-1}s$ . The point marks the critical shear stress defined by equation (12).

value. He defined a critical stress  $\sigma_c$  separating these two regimes, which can be calculated as:

$$\sigma_c = \frac{1}{\sqrt{K_0 \lambda \varphi_\infty (1 - 2\varphi_0/\varphi_\infty)}}. \quad (12)$$

This critical stress value is marked in figure 1(a) by a black circle. At small values of  $\varphi_0$ , an *apparent yield stress* is observed, and at  $\varphi_0 = 0$ , the first Newtonian region (located at low values of shear rate) vanishes and a non-zero stress  $\sigma_y$  is found even for vanishing values of shear rates:

$$\sigma_y = (K_0 \lambda \varphi_\infty)^{-1/2}. \quad (13)$$

Calderas [19] and his team showed experimentally that the yield stress measured for Kaolin suspensions can be modelled using the BMP model.

### 2.2.2 Fluidity and first normal stress difference coefficient

The BMP model exhibits plateaus at low and high shear rates for both the fluidity  $\varphi$  and the first normal stress difference coefficient  $\Psi_1$  (shown in figures 1(b) and 1(c)). We can think of a viscoelastic relaxation time  $\tau$  defined via the shear viscosity as

$$\tau = \frac{\eta}{G_0} = \frac{1}{G_0 \varphi}; \quad (14)$$

in that case, the normal stress coefficient is

$$\Psi_1 = \frac{2\eta^2}{G_0} = 2G_0\tau^2. \quad (15)$$

In the transition region, if we fit the fluidity curve with a power law  $\varphi \sim \dot{\gamma}^{1-n}$  then  $\tau$  will follow the same power law and it follows that  $\Psi_1$  grows as  $\dot{\gamma}^{2(1-n)}$ .

Returning to the plateaus, we can use equation (10) to estimate the range of shear rates applying to each:

$$\varphi \approx \varphi_0 \text{ when } \dot{\gamma}^2 \ll \frac{\varphi_0}{K_0 \lambda}; \quad \varphi \approx \varphi_\infty \text{ when } \dot{\gamma}^2 \gg \frac{\varphi_\infty}{K_0 \lambda}. \quad (16)$$

## 2.3 Dimensionless form of the governing equations

We consider a two-dimensional channel flow of a fluid that satisfies equations (1)–(7). The channel has an infinite extent in  $x$ -direction, and has half-height  $L$ . The fluid is driven by a pressure gradient  $\mathcal{P}$  in the  $x$ -direction, and flows with centreline velocity  $U_0$ . The dimensionless flow geometry is sketched in figure 2.

We scale lengths with  $L$ , times using the average shear rate  $U_0/L$ , and fluidities with the high-shear rate value  $\varphi_\infty$ . The natural stress scale then becomes

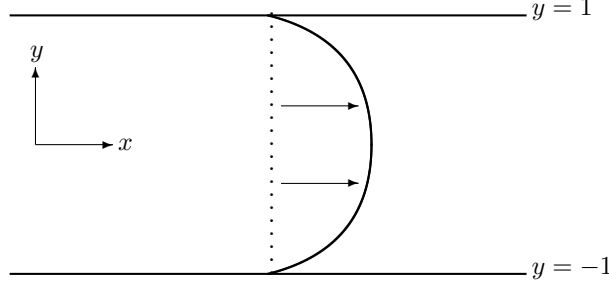


Figure 2: Schematic of two-dimensional channel flow. The pressure gradient drives flow from left to right; the fluid obeys no-slip boundary conditions at the walls.

$\varphi_\infty^{-1}(U_0/L)$ . In terms of dimensionless variables, the governing equations become:

$$\nabla \cdot \underline{u} = 0 \quad (17)$$

$$Re \left( \frac{\partial \underline{u}}{\partial t} + \underline{u} \cdot \nabla \underline{u} \right) = -\nabla P + \nabla \cdot \underline{\underline{\sigma}}} \quad (18)$$

$$\underline{\underline{\sigma}}} + \frac{W}{\varphi} \underline{\underline{\sigma}}} = \frac{2}{\varphi} \underline{\underline{D}}} \quad (19)$$

$$\frac{D\varphi}{Dt} = \frac{1}{\Lambda} (\Phi - \varphi) + \Gamma (1 - \varphi) \underline{\underline{\sigma}}} : \underline{\underline{D}}} \quad (20)$$

Five dimensionless numbers appear in our system of equations, being the well-known Reynolds number  $Re$  and Weissenberg number  $W$ :

$$Re = \rho U_0 L \varphi_\infty \quad W = \lambda_{ve} \left( \frac{U_0}{L} \right) = \frac{1}{G_0 \varphi_\infty} \left( \frac{U_0}{L} \right). \quad (21)$$

along with the extra parameters required by the model:

$$\Phi = \frac{\varphi_0}{\varphi_\infty} = \frac{\eta_\infty}{\eta_0} \quad \Lambda = \lambda \left( \frac{U_0}{L} \right) \quad \Gamma = \left( \frac{1}{\varphi_\infty} \frac{U_0}{L} \right) K_0 \quad (22)$$

$\Phi$ , the *thixotropic ratio*, is simply the ratio between zero and high shear rate fluidities. Despite its simplicity, this dimensionless number is highly important to distinguish between shear-thinning ( $\Phi < 1$ ) and shear-thickening ( $\Phi > 1$ ) fluids. The thixotropic ratio is analogous to the exponent  $n$  used in power-law models [3]; both indicate the strength the shear-thinning behaviour: for low values of both parameters ( $\Phi$  and  $n \ll 1$ ) we have a strongly shear-thinning fluid. The remaining parameters  $\Lambda$  and  $\Gamma$  are timescale and stress ratios, which we discuss in the following sections. They are crucial in defining the key dimensionless quantities of thixo-elasto-plasticity: the thixoelastic, thixoplastic and elastoplastic numbers.

### 2.3.1 Thixoviscous and thixoelastic numbers

A recently published paper by Ewoldt and McKinley [6] shows how plasticity and thixotropy can be incorporated with viscoelasticity. Each one of these complex rheological behaviours has a characteristic timescale. These timescales allow us to form dimensionless groups that can be mapped into a three dimensional space to represent thixotropic elastoviscoplastic material responses. In this section we form Ewoldt and McKinley's three dimensionless groups for the BMP model.

The first grouping is  $\Lambda$ , as defined in equation (22), and is the ratio of the fluid's reformation time to a typical flow time. It is known as the *thixoviscous number*; its form looks similar to the Weissenberg number of equation (21), but critically, the timescale  $\lambda$  here is not the viscoelastic relaxation time but the time over which structure recovers from flow. For high values of the thixoviscous number ( $\Lambda \rightarrow \infty$ ), the fluid will exhibit a slow or null recovery of viscosity after the cessation of flow; fast structural recovery is seen for the opposite case ( $\Lambda \rightarrow 0$ ).

The next grouping is the *thixoelastic number*. There is often confusion in the literature between non-ideal thixotropy and nonlinear viscoelasticity. Larson [7] states that pure thixotropic behaviour can only occur when the viscoelastic relaxation time  $\lambda_{ve}$  is much shorter than the thixotropic timescale  $\lambda$ . We define the thixoelastic number as

$$W_{te} = \frac{\lambda_{ve}}{\lambda} = \frac{W}{\Lambda}. \quad (23)$$

Large values of  $W_{te}$  correspond to pure viscoelasticity, with any thixotropic response happening very quickly; strong thixotropy is the opposite limit  $W_{te} \rightarrow 0$ .

### 2.3.2 Dimensionless critical stress and thixoplastic number

The parameter  $\Gamma$  in equation (22) is associated with the destruction or breaking down of structure.  $K_0$  has units  $(\text{stress})^{-1}$ , which indicates that  $\Gamma$  is in some way a ratio of stresses. When we come to solve for steady channel flow, the parameter  $\Gamma$  only appears in the combination  $\Gamma\Lambda$ , which has been defined by Herrera [27] as the ratio between viscous work and kinetic structural work:

$$\Gamma\Lambda = \frac{\eta_{\infty}(U_0/L)^2}{(K_0\lambda)^{-1}}. \quad (24)$$

This means that for high values of  $\Gamma\Lambda$  the structural destruction dominates over reformation and we have a highly thixotropic material. For small  $\Gamma\Lambda$ , we have either weak destruction or quick structural reformation.

For a steady, homogeneous flow, the limit  $\Lambda \rightarrow \infty$  (no fluidity recovery) yields a viscoelastic fluid having a dimensionless fluidity equal to 1 (i.e. a value

of the dimensional fluidity equal to the high-shear rate fluidity,  $\varphi_\infty$ ). If, on the other hand, the destruction parameter  $\Gamma = 0$  (this is no breaking down of structures), we have a similar scenario: a viscoelastic fluid but with a fluidity  $\varphi_0$ .

The dimensionless form of the critical stress in (12) can be defined in terms of  $\Gamma$ ,  $\Lambda$  and  $\Phi$ :

$$\tau_c = \frac{1}{\sqrt{\Gamma\Lambda(1-2\Phi)}}. \quad (25)$$

If the product  $\Gamma\Lambda$  is large, only a small stress is required to destroy the complex structural networks. Note that yield stress behaviour is recovered when  $\Phi = 0$ , and equation (25) is reduced to:

$$\tau_y = (\Gamma\Lambda)^{-1/2}. \quad (26)$$

As discussed in [6], for thixo-plastic fluids in which the (apparent) yield stress  $\sigma_c$  or  $\sigma_y$  is re-established after the cessation of flow, we can define the (dimensionless) timescale over which this process occurs:

$$\lambda_{tp} = \frac{\eta_\infty}{\sigma_c} \quad W_{tp} = \lambda_{tp} \left( \frac{U_0}{L} \right) = \sqrt{\Gamma\Lambda(1-2\Phi)}. \quad (27)$$

This new dimensionless number  $W_{tp}$  is the *thixoplastic number*, and is simply the inverse of the Bingham number. If  $W_{tp} \rightarrow 0$ , an apparent yield stress is observed; for higher values of  $W_{tp}$  the recovery of critical stress after flow is slower, and in the limit  $W_{tp} \rightarrow \infty$  no critical stress is observed.

We have now derived all the dimensionless groups described in [6] in terms of our dimensionless numbers from equation (22). Of course, other combinations of these can be made; but these three parameters  $\Lambda$ ,  $W_{te}$  and  $W_{tp}$ , serve to link our results to the framework introduced by [6].

### 3 Stability calculation

#### 3.1 Base state

We consider a two-dimensional channel flow (see figure 2) of infinite extent in the  $x$ -direction, dimensionless height 2 (in the  $y$ -direction) and driven by a dimensionless constant pressure gradient  $\mathcal{P}$  in the  $x$ -direction. We assume a steady, unidirectional flow profile  $\underline{u} = U(y)\underline{e}_x$  satisfying a no-slip condition at  $y = \pm 1$ . Under these conditions, and denoting  $U' = dU/dy$ , equations (17)–(20) become:

$$0 = \mathcal{P} + \frac{d\sigma_{12}}{dy} \quad (28)$$

$$\sigma_{12} = \frac{1}{\varphi} \frac{dU}{dy} \quad \varphi = \frac{\Phi + \Gamma\Lambda\sigma_{12}U'}{1 + \Gamma\Lambda\sigma_{12}U'}. \quad (29)$$

Equation (28) immediately gives:

$$\sigma_{12} = -\mathcal{P}y + C, \quad (30)$$

where we can discard the constant  $C$  by symmetry arguments. Substituting equation (30) into equation (29), we obtain an equation for the velocity gradient:

$$\dot{\gamma}_0 = |U'| = \frac{1}{2}\mathcal{P}y - \frac{1}{2\Gamma\Lambda\mathcal{P}y} \pm \frac{\sqrt{by^4 - cy^2 + 1}}{2\Gamma\Lambda\mathcal{P}y}, \quad (31)$$

in which

$$b = \Gamma^2\Lambda^2\mathcal{P}^4, \quad c = 2W_{tp}^2\mathcal{P}^2 = 2\Gamma\Lambda(1 - 2\Phi)\mathcal{P}^2. \quad (32)$$

Equation (31) (which has only one physically possible root) is the analytic form of the shear rate  $\dot{\gamma}_0$ . For the case no structural breakdown, or of fast recovery, we are in the limit  $\Gamma\Lambda = 0$  and equation (31) is reduced to  $\dot{\gamma}_0 = \Phi\mathcal{P}|y|$ , which is the profile of a Maxwell fluid with our low-shear viscosity. In that case we have a simple velocity profile  $U = (1/2)\Phi\mathcal{P}(1 - y^2)$ . In the opposite limit of null structural relaxation  $\Gamma\Lambda \rightarrow \infty$  the fluid takes on the high-shear viscosity and the shear rate and velocity profiles are  $2|y|$  and  $(1 - y^2)$ , respectively.

Integrating equation (31) and applying the no-slip boundary conditions on the channel walls, we have an analytic equation for the velocity profile:

$$U = \frac{1}{4}\mathcal{P}(1 - y^2) - \frac{1}{4\Gamma\Lambda\mathcal{P}}(U_1 + U_2 + U_3), \quad (33)$$

where:

$$U_1 = \sqrt{by^4 - cy^2 + 1} - \sqrt{b - c + 1} \quad (34)$$

$$U_2 = \frac{c}{2\sqrt{b}} \ln \left[ \frac{2\sqrt{b}\sqrt{b - c + 1} + 2b - c}{2\sqrt{b}\sqrt{by^4 - cy^2 + 1} + 2by^2 - c} \right] \quad (35)$$

$$U_3 = \ln \left[ \frac{2 - c + 2\sqrt{b - c + 1}}{2 - cy^2 + 2\sqrt{by^4 - cy^2 + 1}} \right], \quad (36)$$

with centreline velocity:

$$U_0 = \frac{1}{4}\mathcal{P} - \frac{1}{4\Gamma\Lambda\mathcal{P}} \left( 1 - \sqrt{b - c + 1} + \frac{c}{2\sqrt{b}} \ln \left[ \frac{2\sqrt{b}\sqrt{b - c + 1} + 2b - c}{2\sqrt{b} - c} \right] + \ln \left[ \frac{2 - c + 2\sqrt{b - c + 1}}{4} \right] \right). \quad (37)$$

Equations (33) and (37) allow us to calculate the velocity profile, and along with the fluidity (29) and shear rate (31) equations, we can fully describe the base state for our system. However, the value of the dimensionless gradient pressure

gradient  $\mathcal{P}$  has to be determined numerically to satisfy the constraint that the dimensionless centreline velocity  $U_0$  of equation (37) is equal to 1.

A dimensional equation for the velocity profile and shear rate can be found in appendix A.

## 3.2 Velocity profiles

### 3.2.1 Dependence on the thixotropic ratio

In this section we will illustrate some of the different velocity and fluidity profiles that can be obtained for various values of our model parameters.

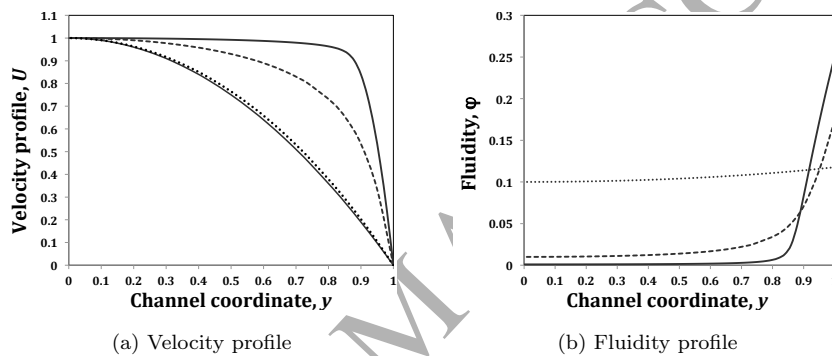


Figure 3: Velocity and fluidity profiles from equations (33)–(36) and (29) with  $\Gamma\Lambda = 0.005$ . For both panels, dotted line ( $\Phi = 0.1$ ), dashed line ( $\Phi = 0.01$ ) and top solid line ( $\Phi = 0.001$ , highly shear-thinning fluid). The bottom solid line in (a) is the velocity profile for the Maxwell case,  $\Phi = 1$ .

In figure 3 we show profiles of velocity and fluidity different values of the thixotropic ratio  $\Phi$ , keeping the structural evolution parameter constant,  $\Gamma\Lambda = 0.0005$ . The bottom solid line in (3a), which we have not included in the fluidity plot, represents the case  $\Phi = 1$ , for which the fluidity is constant: the Maxwell model. As the thixotropic ratio decreases, the curves approach a plug flow near the centreline of the channel; this is most evident for the case when  $\Phi = 0.001$  (solid line), where a Bingham-like behaviour is observed. A higher value of the dimensionless pressure gradient is required to keep the centreline velocity at 1 as  $\Phi \rightarrow 0$ .

We see in figure 3b that the fluidity at the centreline is given by  $\Phi$ ; and that the fluidity increases as we move away from the centreline. For the case  $\Phi = 0.1$  (dotted-line), the fluidity is almost constant across the channel, yielding a nearly-parabolic velocity profile similar to the Maxwell model. For the particular case  $\Phi = 0.001$ , the critical stress  $\tau_c$  (calculated with equation (25)) is reached

within the channel (at  $y \approx 0.867$ ), giving a higher value of fluidity at the wall than the other cases.

### 3.2.2 Extremes of structural destruction and reformation

In this section, we focus on a fixed value of the thixotropic ratio ( $\Phi = 0.001$ , highly shear-thinning) to study the dependence of the velocity and fluidity on the product  $\Gamma\Lambda$ . Since the parameters  $\Gamma$  (structural destruction rate) and  $\Lambda$  (structural reformation timescale) only affect the flow profiles through their product, it follows that the effect of increasing destruction by increasing  $\Gamma$  is *exactly* equivalent to decreasing structural recovery by increasing  $\Lambda$ ; in dimensional terms, for a given material this corresponds to increasing the flow rate.

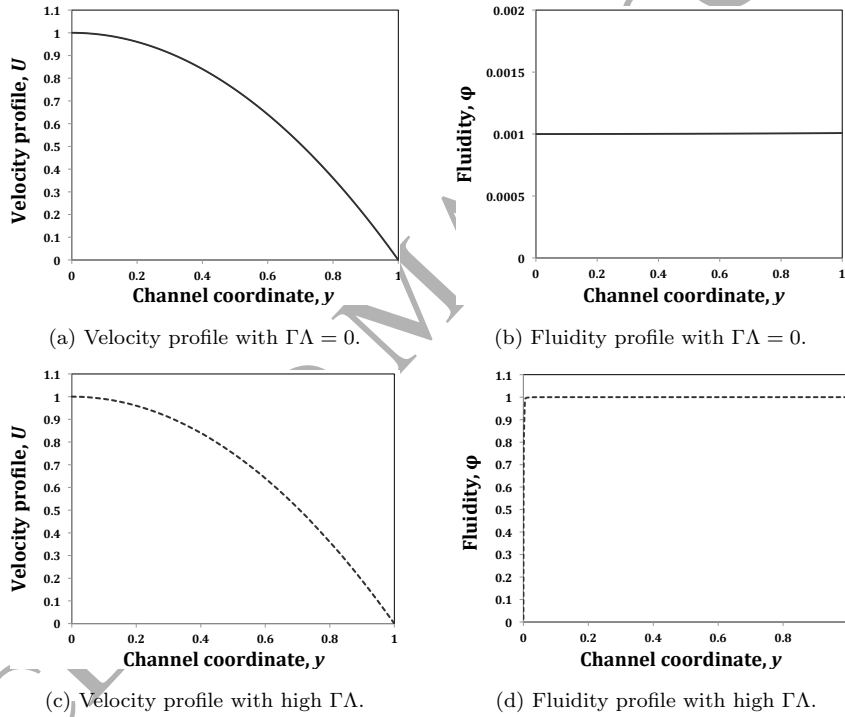


Figure 4: Velocity and fluidity profiles from equations (33)–(36) and (29) with  $\Phi = 0.001$ . Parts a) and b) shows a fluid with extremely quick structural recovery or null destruction,  $\Gamma\Lambda \rightarrow 0$ . Part c) and d) show a fluid that exhibits fast destruction and slow reformation ( $\Gamma\Lambda = 10^6$ ).

In figure 4 we show velocity and fluidity profiles for the two extreme cases. In the case of fast recovery and slow destruction,  $\Gamma\Lambda \rightarrow 0$ , shown in figures (4a)–(4b), the fluidity retains its zero-shear value of  $\Phi$  across the whole channel, giving

constant viscosity and a parabolic velocity profile. Because our  $\Phi = 0.001$  is so small, the fluid is very viscous and we require a large dimensionless pressure gradient  $\mathcal{P} = 2/\Phi$  to drive a flow with unit velocity at the centreline. In the opposite case  $\Gamma\Lambda \gg 1$ , shown in figures (4c)–(4d), there is a very small zone around the centreline where the dimensionless fluidity is equal to  $\Phi = 0.001$  (*unyielded zone*), but the bulk of the channel falls in the *yielded zone*, i.e. the zone where highly oriented structures have been reached and  $\varphi \approx 1$ . Again, the viscosity is constant across almost all of the channel, so the velocity profile is approximately parabolic; but the fluidity is much higher than the previous case so the required pressure gradient is much smaller ( $\mathcal{P} = 2$ ).

### 3.2.3 Strong to moderate destruction

In figure 5 we show velocity and fluidity profiles at  $\Phi = 0.001$ , over a range  $0.025 \leq \Gamma\Lambda \leq 0.4$ . Here the central “plug flow” region where  $\varphi \approx \Phi$ , that we could just make out in figure (4d) when destruction was strong, becomes much wider as the fairly low shear rates near the centre of the channel fail to break down the fluid structure. On the velocity profiles in figure (5a) we have marked the channel location of the critical stress  $\tau_c$  defined in equation (25); we see that it is a good proxy for the edge of the plug flow. As  $\Gamma\Lambda$  decreases, so does the fluidity at the walls.

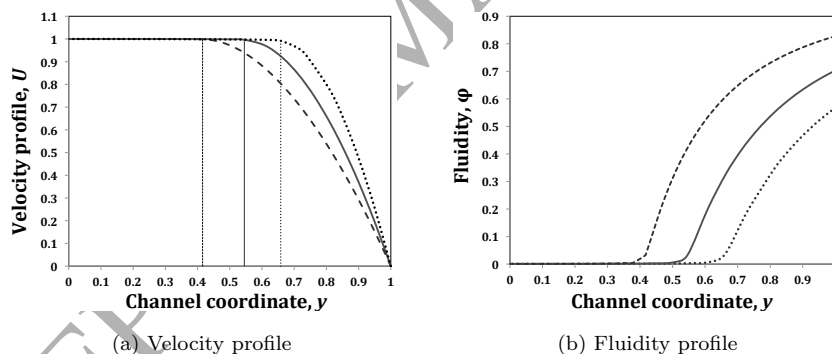


Figure 5: Velocity and fluidity profiles calculated using (33)–(36) and (29) with  $\Phi = 0.001$ . For both figures, dotted line ( $\Gamma\Lambda = 0.025$ ), solid line ( $\Gamma\Lambda = 0.10$ ) and dashed line ( $\Gamma\Lambda = 0.40$ ). The vertical lines in figure (5a) indicate the location of the critical stress  $\tau_c$  calculated with (25).

### 3.2.4 Weak destruction

When the destruction is very weak indeed, or the flow very slow (e.g. the dotted lines in figure 6, which correspond to  $\Gamma\Lambda = 10^{-6}$ ) we do not see a yielded region

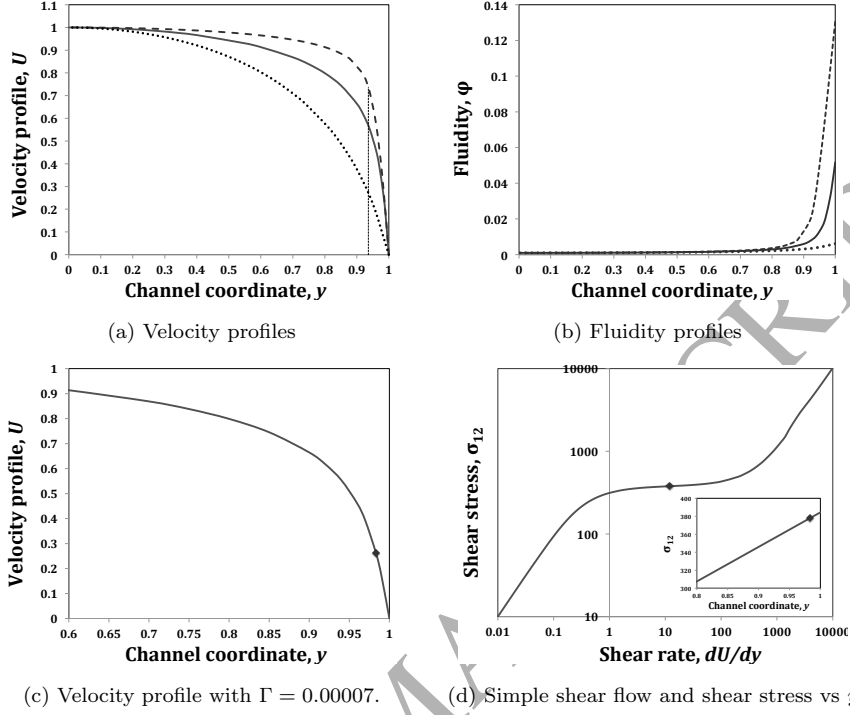


Figure 6: (a) Velocity and (b) fluidity profiles from equations (33)–(36) and (29) with  $\Phi = 0.001$ . Dotted line:  $\Gamma\Lambda = 10^{-6}$ ; solid line  $\Gamma\Lambda = 7 \times 10^{-6}$ ; dashed line  $\Gamma\Lambda = 5 \times 10^{-5}$ . (c) Velocity profile at  $\Gamma\Lambda = 7 \times 10^{-6}$  again, with the critical stress  $\tau_c$  marked; it lies just within the channel at  $y \approx 0.983$ . (d) Flow curve (shear stress against shear rate) for the same parameters as (c), with (inset) the stress profile across the channel.

as the whole channel is below the critical stress. The fluidity is almost constant across the channel and the velocity profile is almost parabolic. If we increase  $\Gamma\Lambda$  to  $7 \times 10^{-6}$ , the critical stress is reached close to the channel wall (as marked in figure (6c)) and the fluidity increases markedly in the wall region. As we increase  $\Gamma\Lambda$  further, this trend continues until eventually (as seen in section 3.2.3) the wall fluidity saturates at a value close to 1.

### 3.3 Equation formulation: perturbation flow

We add an infinitesimal perturbation to the base flow, modifying every flow variable in a similar way (taking velocity as an exemplar):

$$\underline{u} = (U, 0) + \epsilon(\hat{u}, \hat{v}), \quad (38)$$

in which  $\epsilon$  is a small parameter and the perturbation quantities  $\hat{u}$  and  $\hat{v}$  can depend on space and time. We can then expand our governing equations in powers of  $\epsilon$ . Discarding terms of order  $\epsilon^2$  allows us to investigate the *linear* stability of the system. The leading-order terms involve only base-state quantities and are already satisfied. The remaining terms are linear in perturbation quantities, and because the base state variables are independent of  $x$  and  $t$  it is helpful to take a Fourier transform with respect to those variables. We then use the theory of *normal modes* to argue that perturbations of a given wavelength do not interact (at linear order) with those of any other wavelength. This is equivalent to assuming that our perturbation quantities are of the form

$$\hat{u}(x, y, t) = \text{Real}(u(y) \exp[ikx - i\omega t]), \quad (39)$$

in which  $k$  is the (real) wavenumber and  $\omega$  the (complex) frequency.

Our perturbed quantities are then:

$$\underline{u} = (U + u\epsilon, v\epsilon) \quad (40)$$

$$\underline{\underline{\sigma}}^{tot} = \underline{\underline{\sigma}} + \epsilon \underline{\underline{\Sigma}} \quad \underline{\underline{\sigma}}^{tot} = \begin{pmatrix} \sigma_{11} + \Sigma_{11}\epsilon & \sigma_{12} + \Sigma_{12}\epsilon \\ \sigma_{21} + \Sigma_{21}\epsilon & \sigma_{22} + \Sigma_{22}\epsilon \end{pmatrix} \quad (41)$$

$$\varphi' = \varphi + \phi\epsilon \quad (42)$$

$$\underline{\underline{D}} = \underline{\underline{D}}_0 + \underline{\underline{d}}\epsilon, \quad (43)$$

in which all the perturbation quantities are functions of the cross-channel coordinate  $y$ , and  $\epsilon$  denotes a single Fourier mode:

$$\epsilon = \epsilon \exp[ikx - i\omega t]. \quad (44)$$

The continuity equation becomes:

$$iku + Dv = 0, \quad (45)$$

where  $D$  denotes differentiation with respect to  $y$ . In order to reduce one dependent variable, we introduce the streamfunction  $\psi$ , defined as:

$$u = D\psi \quad v = -ik\psi, \quad (46)$$

which automatically satisfies (45). The remaining governing equations become:

$$\text{Re}(-i\omega D\psi - ik\psi DU + ikUD\psi) = ik\Sigma_{11} + D\Sigma_{12} \quad (47)$$

$$\text{Re}(-k\omega\psi + k^2 U\psi) = ik\Sigma_{12} + D\Sigma_{22} \quad (48)$$

$$\phi = \frac{(1 - \varphi)\Gamma [ik\sigma_{11}D\psi + \sigma_{12}(D^2 + k^2)\psi + \Sigma_{12}DU] + ik\psi D\varphi}{(-i\omega + ikU + \Lambda^{-1} + \Gamma\sigma_{12}DU)} \quad (49)$$

$$\Sigma_{22}(-i\omega W\eta + ikUW\eta + 1) = 2\eta(W\sigma_{12}k^2\psi - ikD\psi) \quad (50)$$

$$\begin{aligned} \Sigma_{12}(-i\omega W\eta + ikUW\eta + 1) &= \eta(D^2 + k^2)\psi - \xi DU + ik\psi W\eta D\sigma_{12} \\ &+ W\eta(\sigma_{11}k^2\psi + \Sigma_{22}DU) \end{aligned} \quad (51)$$

$$\begin{aligned} \Sigma_{11}(-i\omega W\eta + ikUW\eta + 1) &= 2\eta ikD\psi - 2W\xi\sigma_{12}DU + ik\psi W\eta D\sigma_{11} \\ &+ 2W\eta(ik\sigma_{11}D\psi + \sigma_{12}D^2\psi + \Sigma_{12}DU) \end{aligned} \quad (52)$$

in which:

$$\xi = \frac{\phi}{\varphi^2} \quad (53)$$

and the base state quantities  $\eta$  and  $\sigma_{ij}$  are:

$$\eta = \varphi^{-1} = \frac{1 + \Gamma\Lambda\sigma_{12}DU}{\Phi + \Gamma\Lambda\sigma_{12}DU} \quad \underline{\underline{\sigma}} = \begin{pmatrix} 2W\mathcal{P}^2y^2 & -\mathcal{P}y \\ -\mathcal{P}y & 0 \end{pmatrix}. \quad (54)$$

Note that if  $W = 0$ , the term  $(-i\omega W\eta + ikUW\eta + 1)$  in equations (50)–(52) is equal to one, in which case the system of equations (47)–(53) would just describe temporal stability analysis for a simple inelastic-thixotropic fluid.

### 3.4 Boundary conditions

The coupled system of equations (47)–(53) can be combined and the resulting equation is a fourth-order ODE in  $\psi$  dependent on  $y$ . The boundary conditions are conditions of no flow on the boundaries:

$$\psi = D\psi = 0 \text{ at } y = \pm 1. \quad (55)$$

This system is governed by six dimensionless parameters: the Reynolds and Weissenberg numbers, the wavenumber  $k$ , the thixotropic ratio  $\Phi$  and the reformation/destruction parameters  $\Lambda$  and  $\Gamma$ . We solve the ODE using the shooting method of Ho & Denn [9].

Previous work on shear-thinning instabilities [3, 4, 5] used power law models, and as a result had to deal with with a singularity in the viscometric functions at the centreline  $y = 0$  where the base-state shear rate is zero. Their solution was to limit themselves to perturbations for which the streamfunction  $\psi$  is an *odd* function of  $y$ , for which the perturbation also has zero shear rate at the centreline. These perturbations are called *varicose* because of the form of the perturbations to streamlines, sketched in figure 7. With the BMP model there is no zero-shear singularity, so we are no longer constrained in which forms of  $\psi$  are allowed.

Since we are solving a linear problem, any solution  $\psi$  can be split into its even and odd components, each of which will also be a solution to our system. For this reason, we will consider separately the two cases of varicose modes ( $\psi$  odd) and sinuous modes ( $\psi$  even), shown in figure 7. For each of these, we can

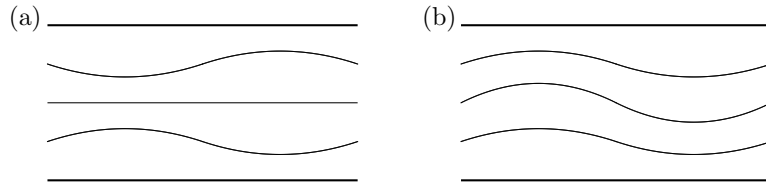


Figure 7: Sketch of the shape of the perturbed streamlines for (a) varicose modes, for which  $\psi$  is an odd function of  $y$ ; (b) sinuous modes, for which  $\psi$  is an even function of  $y$ .

solve over the half-channel  $0 \leq y \leq 1$  with the appropriate symmetry boundary conditions at  $y = 0$ :

$$\psi = D^2\psi = 0 \text{ at } y = 0 \quad \text{for varicose modes,} \quad (56)$$

$$D\psi = D^3\psi = 0 \text{ at } y = 0 \quad \text{for sinuous modes.} \quad (57)$$

The limit  $\Phi = 1$  of our system is the UCM model, whose dispersion relation is well known. We use parameter continuation to obtain the eigenvalue  $\omega$  for any given set of physical parameters.

## 4 Results

### 4.1 Wavelength dependence

#### 4.1.1 Long waves

Wilson [3] expanded  $\omega$  and  $\psi$  in the long wave limit ( $k \rightarrow 0$ ) in terms of  $k$ :

$$\omega = \omega_0 + k\omega_1 + O(k^2) \quad \psi = \psi_0 + k\psi_1 + O(k^2). \quad (58)$$

If we consider the case of small destruction ( $\Gamma \rightarrow 0$ ), the leading order solution ( $k \rightarrow 0$ ) can be obtained from solving equation (51) using the boundary conditions established in (55), which gives the following dispersion relation:

$$\omega_0 = -\frac{i}{W}\Phi, \quad (59)$$

from which we conclude that long waves are stable in this limit, since  $\Phi$  and  $W$  are positive. The Maxwell model solution ( $\Phi = 1$ ) is simply  $\omega_0 = -i/W$ .

The order  $k$  solution is obtained from substituting the leading order quantities into the first order expansion, giving as result a third-order ODE for  $\psi_1$ . For each mode (varicose or sinuous), a characteristic equation is obtained by scaling all the quantities, then taking superposition of the solutions of the ODE and applying their respective boundary conditions [20]. For varicose modes, the

polynomial  $f(\omega_1)$  has four roots that are independent of  $W$ , which were already calculated by Wilson and Renardy [20] :

$$\omega_1 = \begin{cases} 0.29039769 \pm 0.05012283i \\ 0.89882760 \pm 0.12682973i. \end{cases} \quad (60)$$

On the other hand, the characteristic equation for sinuous modes  $g(\omega_1)$  has only two roots, which are:

$$\omega_1 = 0.3257438 \pm 0.171948i. \quad (61)$$

#### 4.1.2 Scaling for short waves

Now we study the other extreme of the wavelengths: the short wave case  $k \rightarrow \infty$ . In this limit, the size of the boundary layer where the shear rate changes near the wall is greater than the wavelength  $O(k^{-1})$ , and therefore, any disturbance will be localised in a region of size  $k^{-1}$ . We therefore scale all lengths with the wavelength, as in [21], and assume that modes will be localised near the channel walls.

We define a new variable  $z$  as  $z = k(y - 1)$ , the symbol  $d$  will denote derivatives w.r.t.  $z$ , and we take the limit  $k^{-1} \rightarrow 0$ . The relevant timescale is the wall shear rate,  $\dot{\gamma}_w$ , and we scale the dimensionless stresses  $\Sigma_{ij}$  by a factor of  $k^2 \dot{\gamma}_w^{-1}$ . Applying these transformations to equations (54)–(53), and assuming  $Re = 0$ , we obtain:

$$\sigma_{12} = -\mathcal{P} \quad \dot{\gamma}_w = -DU_w = \frac{1}{2}\mathcal{P} - \frac{1}{2\Gamma\Lambda\mathcal{P}} + \frac{\sqrt{b-c+1}}{2\Gamma\Lambda\mathcal{P}} \quad (62)$$

$$\eta_w = \frac{1}{\varphi_w} = \frac{1 + \Gamma\Lambda\mathcal{P}\dot{\gamma}_w}{\Phi + \Gamma\Lambda\mathcal{P}\dot{\gamma}_w} \quad \mathcal{W} = W\eta_w \quad (63)$$

$$\chi = -i\omega\dot{\gamma}_w^{-1} - iz + \Lambda^{-1}\dot{\gamma}_w^{-1} - \Gamma\mathcal{P} \quad (64)$$

$$\Theta = \frac{(1 - \varphi_w)\Gamma}{\chi\varphi_w^2\dot{\gamma}_w} [2i\mathcal{W}\mathcal{P}\dot{\gamma}_w d\psi - \mathcal{P}(d^2 + 1)\psi] \quad (65)$$

$$\zeta = \frac{(1 - \varphi_w)\Gamma [2i\mathcal{W}\mathcal{P}\dot{\gamma}_w d\psi - \mathcal{P}(d^2 + 1)\psi - \Sigma_{12}]}{\dot{\gamma}_w\varphi_w^2\chi} \quad (66)$$

$$\Sigma_{22}(-i\omega\dot{\gamma}_w^{-1} - iz + \mathcal{W}^{-1}\dot{\gamma}_w^{-1}) = -2\mathcal{P}\psi - \frac{2i}{\mathcal{W}}d\psi \quad (67)$$

$$\begin{aligned} \Sigma_{12}(-i\omega\dot{\gamma}_w^{-1} - iz + \mathcal{W}^{-1}\dot{\gamma}_w^{-1} + (1 - \varphi_w)\Gamma\mathcal{W}^{-1}\varphi_w^{-2}\chi^{-1}) &= \frac{1}{\mathcal{W}}(d^2 + 1)\psi \\ &- \Sigma_{22} + 2i\mathcal{W}\mathcal{P}\dot{\gamma}_w\psi - \mathcal{W}^{-1}DU_w\Theta \end{aligned} \quad (68)$$

$$\Sigma_{11}(-i\omega\dot{\gamma}_w^{-1} - iz + \mathcal{W}^{-1}\dot{\gamma}_w^{-1}) = \frac{2}{W}id\psi - 2\dot{\gamma}_w^2\zeta + 4i\mathcal{W}\mathcal{P}\dot{\gamma}_w d\psi - 2\mathcal{P}d^2\psi - 2\Sigma_{12}, \quad (69)$$

$$(d^2 + 1)\Sigma_{12} + id(\Sigma_{11} - \Sigma_{22}) = 0 \quad (70)$$

with boundary conditions:

$$\psi(0) = d\psi(0) = 0 \text{ and } \psi \rightarrow 0 \text{ as } z \rightarrow -\infty. \quad (71)$$

As before, the limit  $\Phi = 1$  reduces to the Maxwell model, which is stable. We show results for this short-wave calculation in figure (9a) along with the results for other wavelengths.

We have assumed here that short-wave modes will localise near the channel wall. However, there are other possibilities: in particular, we will see later that there is some potential for modes that localise close to the position where the base state attains the critical stress  $\tau_c$ .

#### 4.1.3 Intermediate waves: sinuous and varicose modes

We use numerical parameter continuation to find the eigenvalue  $\omega(k)$  for each new set of physical parameters. Our starting point is the long-wave results of equations (59) and (60) or (61) for the UCM model. In figure 8 we show this dispersion relation for the UCM model, calculated using our BMP code with  $\Phi = 1$ . These results agree with those already available in the literature [3].

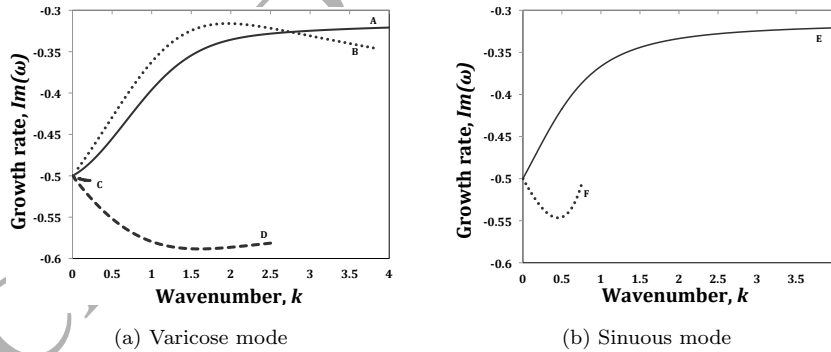


Figure 8: Growth rate against wavenumber for both varicose and sinuous modes for a UCM model, calculated using the BMP model parameters:  $W = 2$ ,  $\Lambda = 1$ ,  $\Phi = 1$  and  $\Gamma = 0.0005$ . Inertia is neglected ( $Re = 0$ ).

For varicose modes, there are four stable modes for very long waves. Two of them (C and D) cease to exist at small  $k$  (one of them at  $k \approx 0.5$ , and the other one at  $k \approx 2.5$ ). The two remaining roots are still seen at longer values of

wavenumber; one of them (A) matches the short-wave solution for a wall mode, while root B localises around the centreline as  $k \rightarrow \infty$ .

Two roots are seen for sinuous modes in figure 8b; one root (F) vanishes at small  $k$ , while the other (E) still exists at large values of the wavenumber. Root E is less stable than root A, but they are equivalent in the limit  $k \rightarrow \infty$ , where wall modes are no longer aware of the centreline boundary conditions.

We use these results as a starting point to move away from the UCM limit  $\Phi = 1$ .

## 4.2 Growth rate as function of the thixotropic ratio

Moving away from the UCM limit, we begin by studying the effect of the thixotropic ratio  $\Phi$  on the growth rate, keeping all other parameters fixed. Initially we look at long waves ( $k = 0.1$ ), with the BMP parameters  $\Lambda = 1$  and  $\Gamma = 0.0005$  and a Weissenberg number of  $W = 2$ . The results are shown in figure 9.

For both sinuous and varicose modes (figures 9a and 9b), decreasing the thixotropic ratio is destabilising; the greater the difference between  $\varphi_0$  and  $\varphi_\infty$ , the more unstable the flow. This is in agreement with earlier work. For sinuous modes (figure 9a) there are initially two roots, but one of them (labelled B) ceases to exist at  $\Phi \approx 0.263$ . The other becomes unstable for values of the thixotropic ratio below 0.043.

We have chosen a small value of  $\Gamma\Lambda = 0.0005$  here; at these values, we saw in section 3.1 that the base state velocity profile is close to plug flow for small values of  $\Phi$ , which is where we now see instability. We cannot calculate growth rates in the true plug flow limit  $\Phi = 0$  because of numerical difficulties associated with the yield stress surface; however, we can approximate it very closely. For the case  $k = 0.1$ , we reached  $\Phi = 5.1 \times 10^{-5}$ , where an instability is still present.

The behaviour for varicose modes is similar to the sinuous behaviour but the detailed picture is more complex as we have at least seven roots. Four remain stable (only three of which are shown in figure 9b as the other ceases to exist at  $\Phi \approx 0.62$ ) but the other three become unstable as  $\Phi$  decreases. We have labelled the most dangerous mode E.

In figure 9c we compare the most dangerous roots (A and E); the sinuous modes are more unstable than the varicose ones here.

Finally, in figure 9d we move away from long waves. Our instability persists as the wavenumber increases, and the root obtained for very short waves has a similar behaviour to roots A and E: the mode remains stable as the thixotropic ratio decreases until  $\Phi$  becomes very small ( $\Phi < 0.046$ ), when an instability appears.

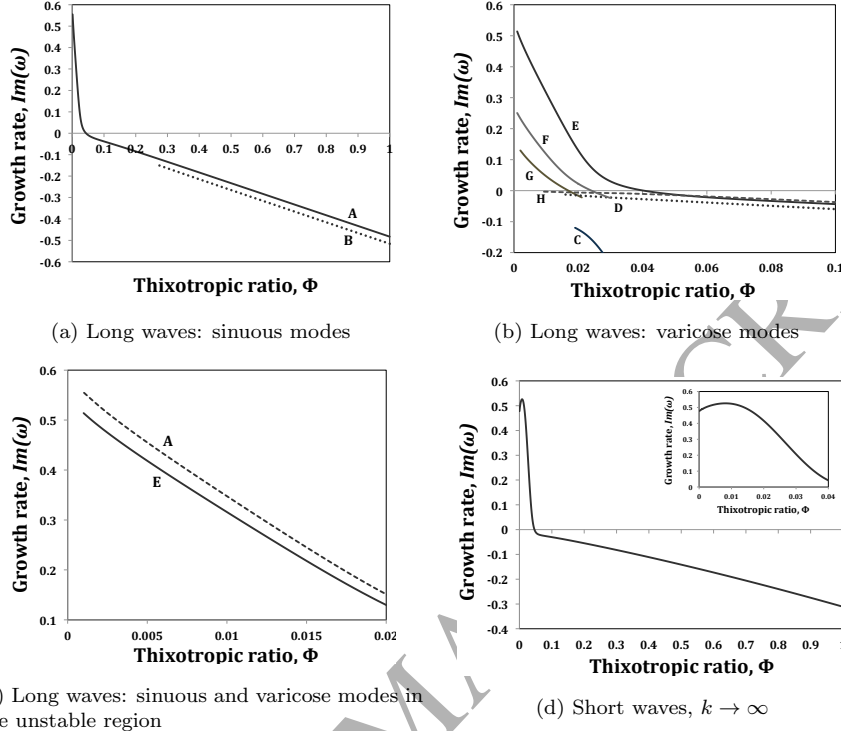


Figure 9: Growth rate plotted against thixotropic ratio, at fixed values of the other parameters:  $W = 2$ ,  $\Lambda = 1$ ,  $\Gamma = 0.0005$  and (a–c) long waves  $k = 0.1$  and (d) short waves  $k \rightarrow \infty$ . (a) Sinuous modes; (b) Varicose modes; (c) Comparison between the two unstable modes at low  $\Phi$ .

However, in the short wave case the growth rate has a maximum value located at  $\Phi \approx 0.007$ , and decreases slightly as we approach  $\Phi \rightarrow 0$  (see inset). We found similar behaviour at moderate wavelengths  $k > 1$ .

### 4.3 Most dangerous wavenumber

In figure 10 we fix our physical parameters (using three sample values of  $\Phi$ ) and vary the wavelength. We see that very long waves ( $k \rightarrow 0$ ) are always stable, but as the wavenumber increases, the flow can become unstable. For the roots with the smaller values of  $\Phi$  (upper curves), the curve passes through a maximum value (most dangerous wavenumber) in the range  $0.35 < k < 0.6$  the growth rate then decreases for shorter waves until it reaches an asymptotic values which matches the short-wave limit solution calculated from equations (62)–(71).

In all cases, the real part of the eigenvalue  $\Re(\omega)$  remains finite as the

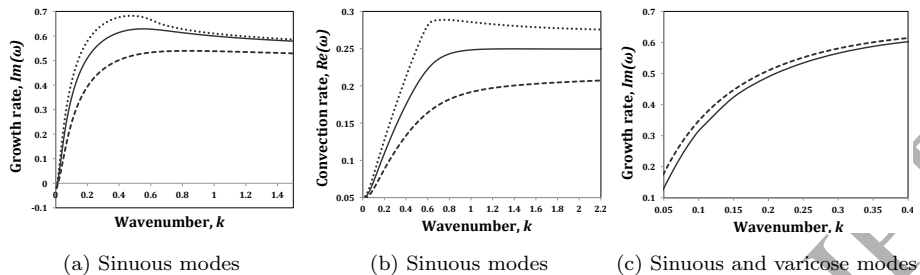


Figure 10: Plots of the eigenvalue  $\omega$  against wavenumber  $k$  for different values of thixotropic ratio. Parameters:  $W = 2$ ,  $\Lambda = 1$ ,  $\Gamma = 0.0005$ . Left: sinuous modes, with  $\Phi = 0.007, 0.01, 0.015$  (top to bottom): (a) growth rate (imaginary part of  $\omega$ ) and (b) convection rate (real part of  $\omega$ ); Right (c): comparison between sinuous modes (dashed line) and varicose modes (solid line) at  $\Phi = 0.01$ .

wavenumber tends to infinity (figure 10b), which means that the short wave perturbations are localised in the wall region and therefore follow the scaling proposed in section 4.1.2.

In figure 10c we compare the curve of growth rate against wavenumber for the most unstable sinuous and varicose perturbations with  $W = 2$ ,  $\Lambda = 1$ ,  $\Gamma = 0.0005$  and  $\Phi = 0.01$ . As before, we see that sinuous modes are more unstable than varicose ones; however, the difference between their growth rates becomes much less significant for shorter waves: at intermediate values of wavenumber  $1 < k < 2$ , the difference is less than 0.32%. We will focus on sinuous modes henceforth.

#### 4.4 Dependence on the Weissenberg number

In this section we show how the Weissenberg number affects the growth rate for different values of thixotropic ratio with the other parameters fixed (figure 11). We are looking at relatively long waves,  $k = 0.1$ , and BMP parameters  $\Lambda = 1$ ,  $\Gamma = 0.0005$ , and three different values of  $\Phi$ . Again, the smaller the value of  $\Phi$  (the stronger the shear thinning), the more unstable the flow is. As the Weissenberg number increases, the instability remains, and the growth rate increases but remains bounded. In all cases small values of the Weissenberg number  $W < 0.15$  yield a stable flow, indicating that elasticity is an important component of the instability.

#### 4.5 Thixotropic timescales

Now that we have identified the range of values for  $\Phi$ ,  $k$  and  $W$  where the instability has its strongest effects, we will discuss the effects of the parameters

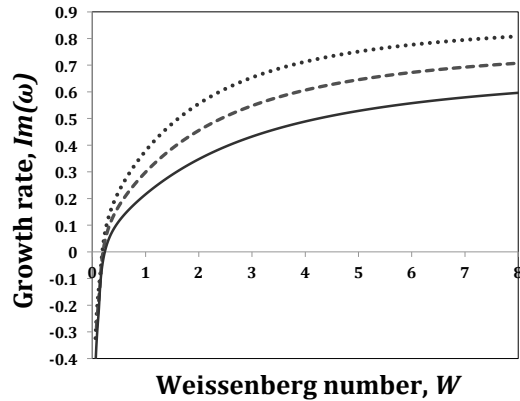


Figure 11: Growth rate against Weissenberg number with  $\Lambda = 1$ ,  $\Gamma = 0.0005$  and  $k = 0.1$ . Bottom to top:  $\Phi = 0.01, 0.005$  and  $0.001$ .

governing structural reformation ( $\Lambda$ ) and destruction ( $\Gamma$ ).

#### 4.5.1 Thixoviscous number $\Lambda$

In figure 12 we plot the growth rate against the thixoviscous number  $\Lambda$  for different values of the thixotropic ratio  $\Phi$ , with  $W = 2$ ,  $\Gamma = 0.0005$  and  $k = 0.1$  fixed.

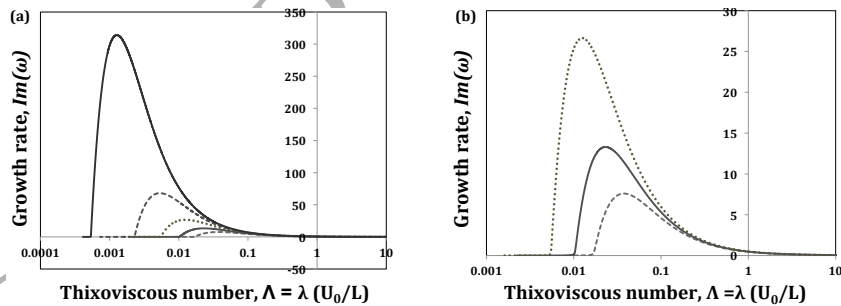


Figure 12: Growth rate plotted against the thixoviscous number  $\Lambda$  for  $W = 2$ ,  $\Gamma = 0.0005$  and  $k = 0.1$ . (a) Bottom to top:  $\Phi = 0.005, 0.004, 0.003, 0.002$  and  $0.001$ . (b) Lower three curves from (a) for clarity.

The flow is linearly stable at both extremes of the thixoviscous number: both for  $\Lambda > 30$ , which applies highly thixotropic fluids (slow structural recovery) and in the limit  $\Lambda \rightarrow 0$  (rapid structural relaxation, a Maxwell fluid). However, for intermediate values of  $\Lambda$  we see an instability with an extremely high growth

rate, which is higher for smaller values of  $\Phi$ . Both the maximum growth rate and the value of  $\Lambda$  at which this growth is seen, vary with the thixotropic ratio  $\Phi$ .

We see this instability for flows in which the critical stress  $\tau_c$  is either located near the wall or has not been reached within the channel; as we reduce  $\Lambda$  the thixoplastic number  $W_{tp}$  reduces and the critical stress increases relative to the stress in the channel. In the limit  $\Lambda \rightarrow 0$ , we regain the Maxwell limit and the instability vanishes.

#### 4.5.2 Thixoelastic number

The thixoelastic number (section 2.3.1) is defined as  $W_{te} = W/\Lambda$  the ratio between the viscoelastic  $\lambda_{ve}$  and structural relaxation times  $\lambda$ . Unlike the parameter  $\Lambda$  itself, the thixoelastic number is a material parameter which does not depend on the timescale of the flow.

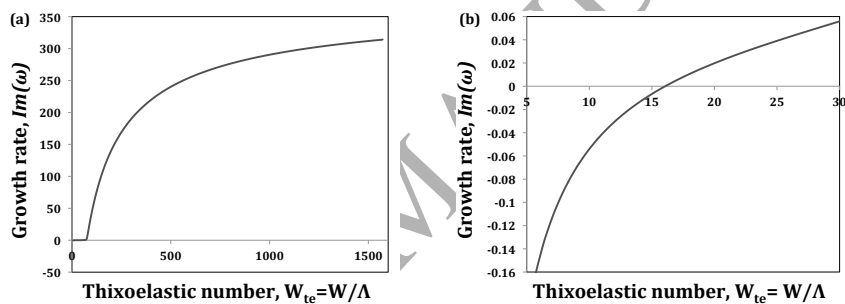


Figure 13: Effect of the thixoelastic number on the instability. Fixed parameters:  $\Lambda = 0.001271$ ,  $\Gamma = 0.0005$ ,  $\Phi = 0.001$  and  $k = 0.1$ ; the Weissenberg number varies. Part (b) is a small region of (a).

We choose our parameters to include the maximum growth rate in figure 12:  $W = 2$ ,  $\Lambda = 0.001271$ ,  $\Gamma = 0.0005$ ,  $\Phi = 0.001$  and  $k = 0.1$ , then allow the Weissenberg number to vary. We plot the resulting growth rates against the thixoelastic number  $W_{te}$  in figure 13.

Large values of the thixoelastic numbers lead to the highest growth rates. In these cases, the relaxation time associated with elastic recoil,  $\lambda_{ve}$ , is much longer than the structural relaxation time  $\lambda$ . This is the case, according to Larson, where the fluid will exhibit complex non-linear viscoelasticity rather than non-ideal thixotropy. This verifies our earlier conclusions [5]: that the instability initially predicted by Wilson and Rallison is purely elastic in nature. Here, though, we have captured sinuous modes, which are the perturbations most commonly observed in experiments.

The growth rate remains positive for  $W_{te} \geq 15.72$ , below which the instabil-

ity vanishes (see figure 13b). Here, though  $\lambda_{ve} > \lambda$ , the viscoelastic effects are less dominant. When structural recovery is slower than viscoelastic relaxation,  $W_{te} < 1$ , the flow is unconditionally stable.

#### 4.5.3 Destruction parameter $\Gamma$ ; thixoplastic number

In figure 14 we fix the thixoviscous number  $\Lambda = 1$  and study the effect of the destruction parameter  $\Gamma$  on the growth rate. These results can also be framed in terms of the thixoplastic number  $W_{tp} = \sqrt{\Gamma\Lambda(1-2\Phi)}$ , since both  $\Lambda$  and  $\Phi$  are constant for each curve.

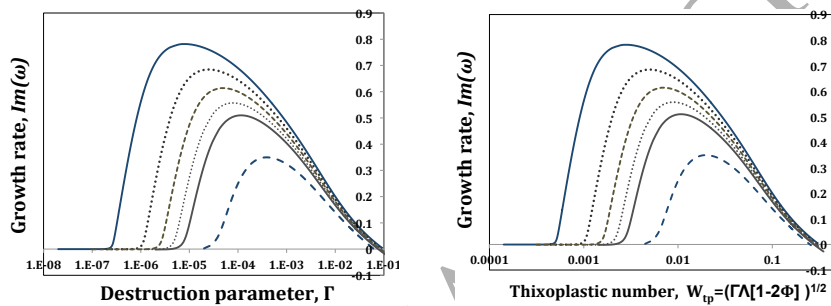


Figure 14: Growth rates at fixed  $W = 2$ ,  $\Lambda = 1$  and  $k = 0.1$  with  $\Gamma$  varying. (a) Growth rate  $\Im(\omega)$  against destruction parameter  $\Gamma$ ; (b): Growth rate against thixoplastic number  $W_{tp}$ . Top to bottom:  $\Phi = 0.001, 0.002, 0.003, 0.004, 0.005$  and  $0.01$ .

There is an unstable maximum for each root, and the limits  $\Gamma \rightarrow 0$  and  $\Gamma \rightarrow \infty$  stabilise the flow. These stable limits are to be expected as either limit reduces to a Maxwell fluid (albeit with very different viscosities), which is stable.

When we plot against the thixoplastic number  $W_{tp}$  the figure looks similar but the interpretation changes: constant values of  $W_{tp}$  mean fixed base state velocity profiles. As we increase  $W_{tp}$  beyond the most dangerous value, the yielded region near the walls grows, and this is associated with a decrease in growth rate. However, there is a most dangerous value of  $W_{tp}$ , associated with a most dangerous flow profile. In the case  $\Phi = 0.001$ , the maximum growth rate occurs when  $W_{tp} = 0.0028$ , a case where we have a small yielded region and the critical stress  $\tau_c$  in the base state is located near the wall, at  $y \approx 0.98$ .

#### 4.5.4 Thixoplastic number at fixed thixoviscous number

In the previous section, we observed that intermediate values of thixoplastic number can destabilise flows as long as the viscoelastic time scale is greater than the structural reformation one ( $W_{te} = W/\Lambda \gg 1$  or  $\lambda_{ve} \gg \lambda$ ). However,

we should note that the thixoplastic number  $W_{tp}$  depends on both  $\Gamma$  and  $\Lambda$ , but in section 4.5.3 we kept the structural reformation parameter fixed at  $\Lambda = 1$ . In this section, we will study the effect of the thixoplastic number on the growth rate with multiple combinations of the destruction and reformation parameters.

We take a set of fixed values for  $\Lambda = \{0.1, 0.2, 0.5, 1, 2, 10\}$ . In each case we calculate the growth rate as function of the thixoplastic number, by varying the destruction parameter  $\Gamma$ . The results can be seen in figure 15a.

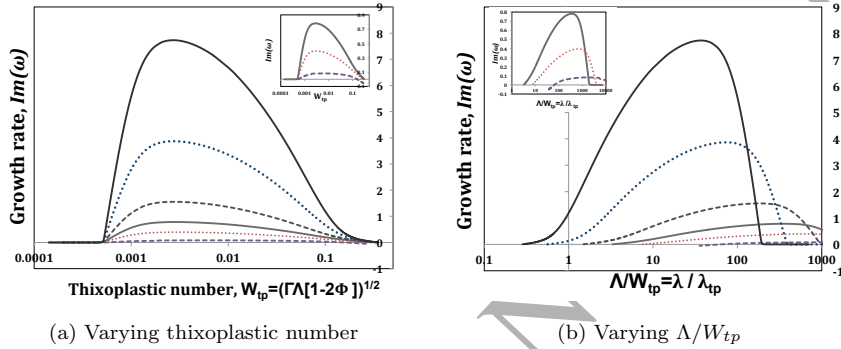


Figure 15: Dependence of growth rate on thixoplastic number, at fixed  $W = 2$ ,  $\Phi = 0.001$  and  $k = 0.1$ . For each curve  $\Lambda$  is constant and  $\Gamma$  varies. Main plots, top to bottom:  $\Lambda = 0.1, 0.2, 0.5, 1, 2$  and  $10$ . Insets, top to bottom:  $\Lambda = 1, 2$  and  $10$ . (a) Growth rate against thixoplastic number; (b): growth rate against the ratio  $\Lambda/W_{tp}$ .

As in figure 14, we see that the extreme limits  $W_{tp} \rightarrow 0$  and large  $W_{tp}$  are stable, and instability can occur for intermediate values. However, we now see a strong dependence of the growth rate of the instability on the reformation parameter  $\Lambda$ . The least unstable curve shown here is  $\Lambda = 10$ , whose maximum value of the growth rate is  $\Im(\omega) \approx 0.08$ , obtained at  $W_{tp} \approx 0.003$ ; but as  $\Lambda$  is decreased, the growth rate increases so that at  $\Lambda = 0.1$  (top solid line in figure 15), the maximum value of growth rate is  $\Im(\omega) = 7.73$  at  $W_{tp} = 0.00269$ . In this most unstable case, the velocity profile in the base state was shown in figure 6c, where we observed an apparent yield region near the channel wall, between  $0.9833 < y < 1$ .

If we consider the most unstable values of  $W_{tp}$  for all the values of  $\Lambda$  in figure 15, in all cases the critical stress  $\tau_c$  is obtained near the wall (at  $y \approx 0.98$ ).

If we reframe these results instead in terms of a material parameter  $\Lambda/W_{tp}$ , which compares the structural relaxation time  $\lambda$  and the time scale associated to the destruction of structures,  $\lambda_{tp}$ , we obtain figure 15b. Now the maximum growth rate shifts to the right as  $\Lambda$  increases; this follows from the universality of the most critical value of  $W_{tp}$  that we saw in figure 15a. For very large values of  $\Lambda/W_{tp}$  the flow tends to be stable; this is a limit where thixotropy dominates

and we reach the high-shear limit across almost all of the channel: the Maxwell limit again. However, if  $\Lambda$  is small (weak thixotropy) we need exceedingly high values of  $\Lambda/W_{tp}$  to attain this limit.

Figure 15 makes it clear that we cannot define stability in terms of material parameters alone: for fixed values of  $k$ ,  $W$  and  $\Phi$  the unstable region is best characterised by  $W_{tp} = \sqrt{\Gamma\Lambda(1-\Phi)}$ , which for our parameter choices gives instability in the range  $0.0005 < W_{tp} < 0.15$ .

We can characterise the unstable region and the most dangerous situation in terms of the thixoplastic number  $W_{tp}$ . For our parameters  $W = 2$ ,  $\Phi = 0.0001$  and  $k = 0.1$  this most dangerous value is  $W_{tp} = 0.002695$ . This value determines the critical stress value ( $\tau_c \approx 370$ ), and its location in the channel (located at  $y \approx 0.9823$ ) which is also the edge of the yielded region. The base-state velocity profile and the flow curve for simple shear are illustrated in figures 6c and 6d for this case.

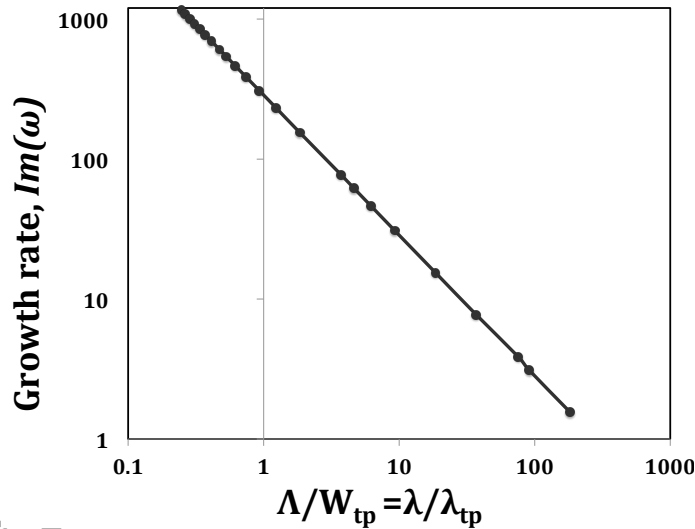


Figure 16: Log-log plot of growth rate plotted against the timescale ratio  $\Lambda/W_{tp}$ . Fixed values  $W = 2$ ,  $\Phi = 0.001$ ,  $k = 0.1$ , and the most dangerous thixoplastic number  $W_{tp} = 0.002695$ . The points are fit with the line  $370.92(\lambda/\lambda_{tp})^{-1}$ .

However, the growth rate of the instability clearly depends on  $\Lambda$  even at fixed  $W_{tp}$ . In figure 16 we use the value above,  $W_{tp} = 0.002695$ , and plot the growth rate against the material parameter  $\Lambda/W_{tp} = \lambda/\lambda_{tp}$ , the ratio of the structural and thixoplastic relaxation times. The curve can be fitted to a power-law equation:  $\Im(\omega) = 370.92(\lambda/\lambda_{tp})^{-1}$  with  $R^2 = 0.9999$ . Thus we can

characterise the growth rate at fixed  $W_{tp}$  (or fixed  $\Gamma\Lambda$ ) by

$$\Im(\omega) \propto \frac{1}{\Lambda} \propto \Gamma. \quad (72)$$

Recall that the base flow is defined by the parameters  $W$ ,  $\Gamma\Lambda$  and  $\Phi$  and does not depend on  $\Lambda$  separately from the combination  $\Gamma\Lambda$ . Thus *for a given unstable base flow*, the rate  $\Lambda^{-1}$  will determine the growth rate of the instability.

Fluids having  $\Lambda/W_{tp} \gg 1$ , i.e. slow structural recovery, will exhibit much weaker instability than those for which structural recovery is fast *given the same base flow*; however, to obtain the same base flow in a fluid having fast structural recovery requires higher flow rates. Though the overall picture is difficult to express briefly in terms of pure material parameters, it is clear that the thixoviscous number  $\Lambda$  is a key player in the strength of the instability.

#### 4.5.5 Elastoplastic number

We have seen that the instability is most dangerous when  $\lambda \ll \lambda_{tp}$  (section 4.5.4) and  $\lambda \ll \lambda_{ve}$  (section 4.5.2). In this section we assess the behaviour of the instability as viscoelastic effects are reduced. We will use the *elastoplastic number*  $\lambda_{ve}/\lambda_{tp} = W/W_{tp}$  to compare the viscoelastic and plastic effects of our fluid. The elastoplastic number is a ratio of two time scales: the relaxation time associated with the elastic recoil of the material chains  $\lambda_{ve}$  over the time scale associated with destruction,  $\lambda_{tp}$ .

The results are shown in figure 17. We see that the instability is present only if the viscoelastic timescale  $\lambda_{ve}$  is much longer than the plastic timescale  $\lambda_{tp}$ , i.e. the elastic recoil process is slow compared to structural destruction,  $W/W_{tp} \gg 1$ . Decreasing the elastoplastic number makes the flow less unstable, until it stabilises at  $W/W_{tp} \approx 8$ , below which the viscoelastic effects are no longer strong enough to cause flow instability.

#### 4.6 Streamfunctions and $x$ -velocity

In this final results section, we show the shape of the streamfunction  $\psi$  (proportional to cross-channel velocity) and  $x$ -velocity  $D\psi$  for both sinuous and varicose perturbations at the most dangerous thixoplastic number.

We choose the values used in figure 16 ( $k = 0.1$ ,  $W = 2$ ,  $\Phi = 0.001$ ) for which the most dangerous thixoplastic number is  $W_{tp} = 0.002695$ . Choosing  $\Lambda = 1$  then fixes  $\Gamma = 7.5 \times 10^{-6}$ . The resulting streamfunctions can be seen in figure 18.

Both sinuous and varicose modes are unstable for these parameters, but the shape of the two streamfunctions is completely different, as one would expect. Most surprising, though, is the peak in the  $x$ -velocity  $D\psi$  for both modes near

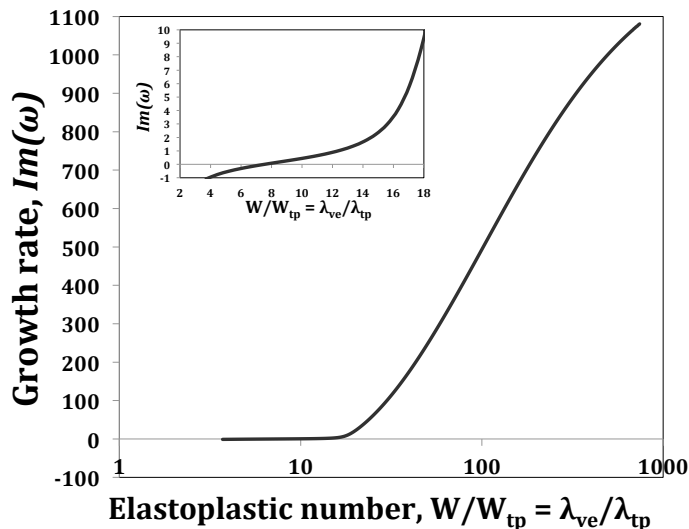


Figure 17: Plot of growth rate  $\Im(\omega)$  against elastoplastic number  $W/W_{tp}$  with fixed values of  $\Phi = 0.001$ ,  $\Gamma = 0.010175$ ,  $\Lambda = 7.143 \times 10^{-4}$  and  $k = 0.1$ .

the channel wall (figures 18c and 18d). This peak occurs roughly where the base state is at the critical stress level  $\tau_c$  (for this fluid at  $y \approx 0.983$ ). At this point, where the gradient  $d\sigma_{12}/d\dot{\gamma}$  of the constitutive curve (figure 6d) is low, the effective viscosity seen by perturbations is also low, so a perturbation can generate large local flows while incurring minimal dissipation of energy.

## 5 Comparison with experiments

In this section, we will briefly compare our results with experiments reported by Bodiguel *et al.* [2], who observed a supercritical instability in microchannel flow of shear-thinning viscoelastic fluids. We begin by finding the BMP model parameters that roughly match the simple shear flow data for their fluid, which was an aqueous solution of polyacrylamide, HPAM (concentration of 4000 ppm and molecular weight of  $18 \times 10^6$  g/mol).

The experimental steady shear flow curve  $\eta(\dot{\gamma})$  allows us to fit our parameters  $\varphi_0$ ,  $\varphi_\infty$  and the combination  $K_0\lambda$ . We then use our shear modulus  $G_0$  to match the experimental first normal stress difference coefficient  $N_1/\dot{\gamma}^2$ . As only steady rheometry is reported by [2], we have no way to determine  $\lambda$  separately from  $K_0$ ; but all the remaining parameters may be derived from combinations of these four parameters determined from the rheology, and simple physical measurements such as the centreline velocity  $U_0$  and the channel half-width  $L$ . The resulting

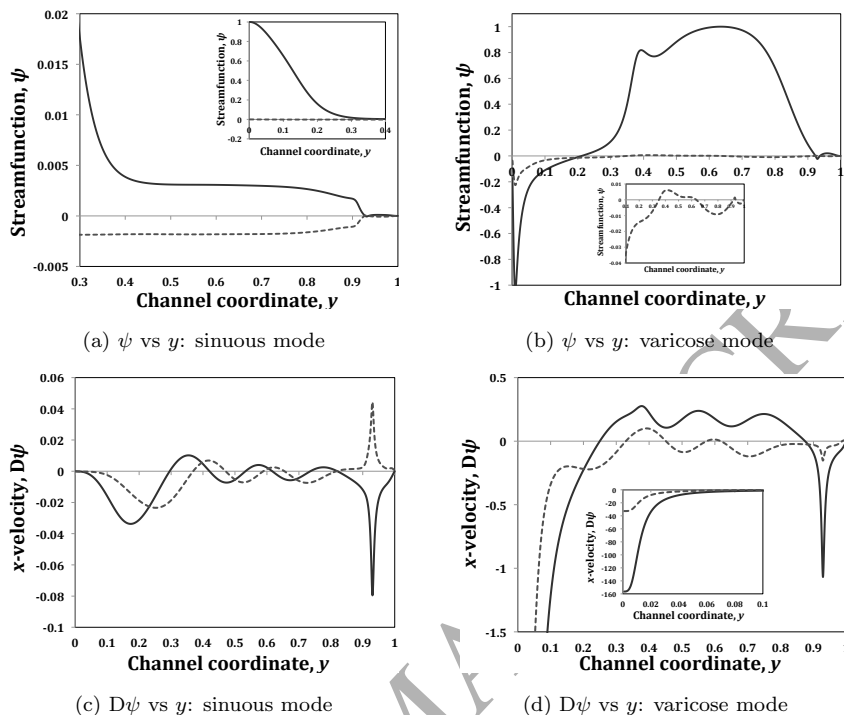


Figure 18: Form of the unstable complex streamfunction  $\psi$  for sinuous and varicose perturbations with  $k = 0.1$ ,  $W = 2$ ,  $\Gamma = 7.5 \times 10^{-6}$ ,  $\Lambda = 1$  and  $\Phi = 0.001$ . The thixoplastic number is  $W_{tp} = 0.002695$ . The curves are normalised so that the maximum value of  $|\psi|$  is 1. For each graph, the solid line is the real part and the dashed line, the imaginary part. Insets show the behaviour near the wall, except in (b) where it shows the shape of the imaginary part of the streamfunction.

parameters are given in table 1.

Similar experiments have been carried out by Poole [16]. The fluid used in those experiments does exhibit a central power-law like behaviour of both viscosity and normal stress for moderate shear rates; however, we cannot fit it with the BMP model. In our model, the first normal stress difference coefficient is  $2\eta^2 G_0^{-1}$ , but Poole's fluid has very different power laws for the viscosity and the first normal stress difference coefficient (or, equivalently, a strongly varying stress modulus). For that reason, we do not attempt a quantitative comparison with Poole's experiments here.

Indeed, even the fit with Bodiguél's fluid is not perfect, as the experimental value of the elastic modulus is not quite constant; however, the parameters given in table 1 give a reasonable match over the range  $0.1 < \dot{\gamma} < 100$ .

Parameter	Value
$\varphi_0$	$0.046 \text{ Pa}^{-1} \text{ s}^{-1}$
$\varphi_\infty$	$10.17 \text{ Pa}^{-1} \text{ s}^{-1}$
$K_0\lambda$	$3.2 \times 10^{-3} \text{ Pa}^{-1} \text{ s}$
$G_0$	$0.455 \text{ Pa}$
$L$	$7.6 \times 10^{-5} \text{ m}$
$\lambda_{ve}$	$0.21 \text{ s}$
$\lambda_{tp}$	$0.017 \text{ s}$
$\Phi$	$0.0045$
$\Gamma\Lambda$	$5.45 \times 10^4 U_0^2$
$W$	$2844 U_0$

Table 1: Physical and dimensionless parameters used to fit our analysis to the experiments of Bodiguel [2], with centreline velocity  $U_0$  in m/s.

From the parameters values shown above, we immediately observe that the thixotropic ratio for the fluid is  $\Phi = 0.0045$ , within the range of values of  $\Phi$  where our theory predicts an instability.

Using the model parameters derived above and for a small set of likely dangerous values of the wavenumber  $k = \{0.1, 0.46, 1\}$ , we look for the *stability boundary*; this is the pressure gradient  $\mathcal{P}$  (or the wall shear stress  $\sigma_w = \mathcal{P}L$ ) above which the flow becomes unstable. Knowing the value of the pressure gradient, we can calculate the dimensional centreline velocity (as in appendix A) and therefore the Weissenberg number and the product  $\Gamma\Lambda$ . As we observed in section 4.5.4, at a fixed value of  $\Gamma\Lambda$ , changing  $\Lambda$  does not affect the stability boundary but rather modifies the growth rate of unstable modes; so we are not affected by our inability to separate  $K_0$  and  $\lambda$  using the fluid rheometry.

We have found that for  $k = 0.1$ , the critical shear stress at the wall  $\sigma_w$  is 5.4609 Pa, meanwhile for  $k = 0.46$  (the most dangerous wavenumber for  $\Phi = 0.0045$ ) it is  $\sigma_w = 4.3593 \text{ Pa}$  and for  $k = 1$  it is  $\sigma_w = 4.2938 \text{ Pa}$ . These results are consistent with the values reported by Bodiguel [2], who found that the critical wall shear stress ranged between 3.5 and 4.7 Pa.

## 6 Conclusions

We have studied the stability in pressure-driven channel flow of materials that exhibit viscoelasto-thixo-plasticity. We used the BMP model, which has been extensively used to describe this kind of complex rheological behaviour using only a modest number of parameters.

We derived an analytic equation for the steady-state velocity profile in channel flow, which depends on physically measurable quantities (such as low and

high shear rate viscosities, structural relaxation time and a structure breakdown parameter).

We obtained a set of dimensionless groups ( $\Phi$ ,  $\Lambda$ ,  $\Gamma$ ) from which we could construct the key dimensionless quantities for analysis of the results in terms of the phenomena of viscoelasticity, thixotropy and plasticity present in our material.

We have made a thorough exploration of the conditions for instability/stability and its growth rate, depending on our model parameters. We have found that viscoelastic effects are the main cause of instability, and that sinuous modes are always more unstable than varicose modes (though sometimes the growth rates of instability are very similar between the modes). We found that a low thixotropic ratio  $\Phi$  (strong shear thinning) is needed to trigger the instability, and identified that the most dangerous wavenumber is located in a range of values of  $0.35 < k < 0.6$ , though the instability persists even at large values of  $k$ , which we validated using short wave calculations. It was not possible to study a fluid with a true yield stress, but the short wave results suggest that the limiting case  $\Phi = 0$  might possibly be stable. Flow stability is seen if either  $k \rightarrow 0$  or  $W \rightarrow 0$  for any value of  $\Phi$ ,  $\Lambda$  and  $\Gamma$ .

We can characterise the instability in terms of the thixoplastic number; in doing so, we found that the instability is strongest if the base-state critical stress  $\tau_c$  is located near the channel-wall (at  $y \approx 0.98$ ).

Under these conditions, the instability grows fastest when the viscoelastic relaxation time  $\lambda_{ve}$  is much longer than both the structural destruction timescale  $\lambda_{tp}$  and the thixotropic timescale  $\lambda$ , and also when the structural destruction occurs over a longer timescale than the thixotropic recovery  $\lambda_{tp} \gg \lambda$ :

$$\lambda \ll \lambda_{tp} \ll \lambda_{ve}. \quad (73)$$

Fluids that satisfy this ordering of timescales exhibit complex non-linear viscoelasticity with shear-thinning characteristics rather than thixotropy, as stated by Larson [7].

Extremes of many parameters cause linearly stable flow: in particular, very large or very small values of the thixoviscous number or the thixoplastic number. Instability is enhanced by large values of the elastoplastic number or the thixoelastic number, which drive the scalings in equation (73) above.

This work leaves some questions open to future work. One is to consider the phenomenon of shear-banding, and compare the interfacial instabilities between shear bands with the bulk instabilities calculated here. More challenging problems are to address the true yield stress case, and to create a model which allows a non-constant shear modulus (to allow both viscosity and normal stress to be fit to experimental measurements) without resorting to *ad hoc* empirical parameters. Finally, a fully comprehensive mechanism for this instability is still elusive, though we have gained valuable insight through the current work.

### Acknowledgements

This work was supported financially by the National Council of Science and Technology of Mexico (CONACyT Grant number: 299629 / 411301). The authors would like to thank Hugh Barlow for useful discussions.

## A Dimensional velocity profile

The steady velocity gradient profile for a BMP model fluid flowing in a two-dimensional channel of infinite extent in the  $x$ -direction and with  $-L \leq y \leq L$  under pressure gradient  $dP/dx = -\mathcal{P}$  is given by

$$\dot{\gamma}_0 = |U'| = \frac{1}{2}\varphi_\infty \mathcal{P} y - \frac{1}{2K_0\lambda \mathcal{P} y} \pm \frac{\sqrt{b_0 y^4 - c_0 y^2 + 1}}{2K_0\lambda \mathcal{P} y}, \quad (74)$$

where the coefficients  $b_0$  and  $c_0$  are:

$$b_0 = K_0^2 \lambda^2 \varphi_\infty^2 \mathcal{P}^4 \quad c_0 = 2K_0\lambda \mathcal{P}^2 (\varphi_\infty - 2\varphi_0). \quad (75)$$

Integrating equation (74) and applying non-slip boundary conditions at the channel-wall ( $y = \pm L$ ), we obtain the velocity profile:

$$U = \frac{1}{4}\varphi_\infty \mathcal{P} (L^2 - y^2) - \frac{1}{4K_0\lambda \mathcal{P}} (U_{01} + U_{02} + U_{03}), \quad (76)$$

where:

$$U_{01} = \sqrt{b_0 y^4 - c_0 y^2 + 1} - \sqrt{b_0 L^4 - c_0 L^2 + 1} \quad (77)$$

$$U_{02} = \frac{1}{2} \frac{c_0}{\sqrt{b_0}} \ln \left[ \frac{2\sqrt{b_0}\sqrt{b_0 L^4 - c_0 L^2 + 1} + 2b_0 L^2 - c_0}{2\sqrt{b_0}\sqrt{b_0 y^4 - c_0 y^2 + 1} + 2b_0 y^2 - c_0} \right] \quad (78)$$

$$U_{03} = \ln \left[ \frac{2 - c_0 L^2 + 2\sqrt{b_0 L^4 - c_0 L^2 + 1}}{2 - c_0 y^2 + 2\sqrt{b_0 y^4 - c_0 y^2 + 1}} \right]. \quad (79)$$

## References

- [1] Bautista, F., de Santos, J.M., Puig, J.E., Manero, O., Understanding thixotropic and antithixotropic behavior of viscoelastic micellar solutions and liquid crystalline dispersions. I. The model, *Journal of Non-Newtonian Fluid Mechanics*, 80 (1999), 93–113.
- [2] H. Bodiguel, A. Beaumont, A. Machado, L. Martinie, H. Kellay and A. Colin, Flow enhancement due to elastic turbulence in channel flows of shear-thinning fluids, *PRL* 114 (2015) 028302.

- [3] H. J. Wilson and J. M. Rallison, Instability of channel flow of a shear-thinning White-Metzner fluid, *Journal of Non-Newtonian Fluid Mechanics* 87 (1999), 75–96.
- [4] H. J. Wilson and V. Loridan, Linear instability of a highly shear-thinning fluid in channel flow, *Journal of Non-Newtonian Fluid Mechanics* 223 (2015), 200–208.
- [5] Castillo, H.A., Wilson, H.J., Towards a mechanism for instability in channel flow of highly shear-thinning viscoelastic fluids, *Journal of Non-Newtonian Fluid Mechanics*, Vol. 247, 2017, pages 15–21.
- [6] Ewoldt, R.H., McKinley, G.H., Mapping Thixo-Visco-Elasto-Plastic Behavior, *Rheological Acta*, March 2017, Volume 56, Issue 3, pp 195–210.
- [7] Larson, R.G., Constitutive equations for thixotropic fluids, *Journal of Rheology*, 59, 595 (2015).
- [8] Fredrickson, A.,G., A model for the Thixotropy of Suspensions, *AICHE Journal*, May 1970, Vol. 16, 16(3):436–441.
- [9] T. C. Ho and M. M. Denn, Stability of plane Poiseuille flow of a highly elastic liquid, *Journal of Non-Newtonian Fluid Mechanics* 3 (1978), 179.
- [10] P.R. de Sousa Mendes, R.L. Thompson, A critical overview of elasto-viscoplastic thixotropic modeling, *Journal of Non-Newtonian Fluid Mechanics*, 187-188, (2012) 8–15.
- [11] R. G. Larson, E. S. G. Shaqfeh, S. J. Muller, A purely elastic instability in Taylor-Couette flow, *JFM* 218 (1990) 573–600.
- [12] P. Pakdel and G. H. McKinley, Elastic instability and curved streamline, *Physical Review Letters*, 77 (1996) 2459–2462.
- [13] E. J. Hinch, O. J. Harris, J. M. Rallison, The instability mechanism for two elastic liquids being coextruded, *JNNFM* 43 (2–3) (1992) 311–324.
- [14] J. C. Miller, J. M. Rallison, Interfacial instability between sheared elastic liquids in a channel, *Journal of Non-Newtonian Fluid Mechanics*, 143 (2-3) (2007) 71–87.
- [15] Wilson, H.J., Fielding, S. M., Linear instability of planar shear banded flow of both diffusive and non-diffusive Johnson-Segalman fluids, *Journal of Non-Newtonian Fluid Mechanics*, 138 (2-3) (2006), 181-196.
- [16] Poole, R.J., Elastic instabilities in parallel shear flows of a viscoelastic shear-thinning liquid, *PRL* 1, 041301(R) (2016).
- [17] Castillo H.A., Castillo Tejas J., García-Sandoval, J., Matus, O., Bautista, F., Puig J.E., Manero, O., Derivation of the mechanical and thermodynamic potentials from the generalized BMP model under shear-banding flow, *Journal of Non-Equilib. Thermodynamics*, 2014; 39 (4), 231-248.

- [18] F. Bautista, J.F.A. Soltero, J.H. Pérez-López, J.E. Puig, O. Manero, On the shear banding flow of elongated micellar solutions, *Journal of Non-Newtonian Fluid Mechanics*, 94 (2000) 57–66.
- [19] Calderas, F., Herrera-Valencia, E.E., Sanchez-Solis, A., Manero, O., Medina-Torres, L., Renteria, A., Sanchez-Olivares, G., On the yield stress of complex materials, *Korea–Australia Rheology Journal*, Springer, Vol. 25, No 4, pp 233–242, November 2013.
- [20] Wilson, H.J., Renardy, M., Renardy, Y., Structure of the spectrum in zero Reynolds number shear flow of the UCM and Oldroyd-B liquids, *Journal of Non-Newtonian Fluid Mechanics*, 80 (1999), 251–268.
- [21] Chen, K.P., Joseph, D.D., Elastic short wave instability in extrusion flows of viscoelastic liquids, *Journal of Non-Newtonian Fluid Mechanics*, 42 (12): 189–211, 1992.
- [22] Renardy, Y., Renardy, M., Stability of shear banded flow for a viscoelastic constitutive model with thixotropic yield stress behavior, *Journal of Non-Newtonian Fluid Mechanics*, 244 (2017) 57–74.
- [23] P.R. de Sousa Mendes, Thixotropic elasto-viscoplastic model for structured fluids, *Soft Matter*, 2011, 7, 2471.
- [24] Mujumdar, A., Beris, A.N., Metzner, A.B., Transient phenomena in thixotropic systems, *Journal of Non-Newtonian Fluid Mechanics*, 102 (2002) 157–178.
- [25] C.J.S. Petrie, M.M. Denn, Instabilities in polymer processing, *A.I.Ch.E.J.* 22 (2) (1976), 209–236.
- [26] Paulo García Sandoval, J, Bautista, F., Puig, J.E., Manero, O., The interface migration in shear-banded micellar solutions, *Rheologica Acta*, (2017) 56, 765–778.
- [27] Herrera-Valencia, E. E., Calderas, F., Medina-Torres, L., Pérez-Camacho, M., Moreno, L., Manero, O., On the pulsating flow behavior of a biological fluid: human blood, *Rheologica Acta*, (2017) 56:387–407.
- [28] Wilson, H., J., Shear flow instabilities in viscoelastic fluids, Dissertation submitted to the University of Cambridge for the degree of Doctor of Philosophy, September 2, 1998, p.262